5-2020

Exploring Pyrochlore Host for Upconversion and Downconversion Luminescence Materials

Mitzy A. Penilla Garcia
The University of Texas Rio Grande Valley

EXPLORING PYROCHLORE HOST FOR UPCONVERSION AND DOWNCONVERSION LUMINESCENCE MATERIALS

A Thesis

by

MITZY A. PENILLA GARCIA

Submitted to the Graduate School of
The University of Texas Rio Grande Valley
In partial fulfillment of the requirements for the degree of
MASTER OF SCIENCE

May 2020

Major subject: Chemistry

EXPLORING PYROCHLORE HOST FOR UPCONVERSION AND DOWNCONVERSION LUMINESCENCE MATERIALS

A Thesis
by
MITZY A. PENILLA GARCIA

COMMITTEE MEMBERS

Dr. Mohammed Jasim Uddin
Chair of Committee

Dr. Karen Lozano
Committee Member

Dr. Tülay Ateşin
Committee Member

Dr. Javier Macossay Torres
Committee Member

May 2020

ABSTRACT

Penilla Garcia, Mitzy A., Exploring pyrochlore host for upconversion and downconversion luminescence materials. Master of Science (MS), May 2020, 59 pp., 4 tables, 23 figures, 85 references.

Pyrochlore has been the focal point of research in the matter science community in the area of nuclear waste host, thermal barrier coatings, solid oxide fuel cell, catalyst, magnetism, luminescence etc. Such application arises due to their unique properties such as wide band gap, high radiation stability, low thermal conductivity, high dielectric constant. The fact it also has high structural ability, low phonon energy and ability to accommodate dopant ion at both A- site and B-site; they are considered excellent hosts for inorganic phosphors. This research work is directed towards synthesizing optical materials having high quantum efficiency for down-conversion (DC) and up-conversion (UC).

Molten salt synthesis because of its several benefits such as low temperature synthesis, friendly environmental process, and low cost are expected to produce high quality cost effective, pyrochlore nanoparticles with $A_2B_2O_7$ which is expected to show high quantum yield due to unique f-f transition of lanthanide ion and host to lanthanide energy transfer. We believe by suitable tuning of dopant ion its concentration, annealing time, annealing temperature, we will be able to produce small size luminescent nanoparticles of $A_2B_2O_7$ for up-conversion and down-conversion suitable by bio imaging and solid-state lighting.

DEDICATION

To my mother, Kathy O. Garcia, that raised me to be strong, to follow my dreams, to be an independent woman, and to have the courage to stand up against adversity. To my daughter, Darina M. Garcia, that taught me that being a single mother was not bad but an incredible choice. Thank you, Darina, for giving me strength and helping me continue my path in the right direction, when I could not see the end of the tunnel. To all the women out there, doubting whether education is worthy or not. Be the woman that knows what she wants, finds it, chases it and finishes it. It is worth it! To Maurilio Soto, thank you for being such an amazing stepfather to our girl and supporting me throughout my career. All the nights, I needed to study late, all the times I could not be at home because I needed to be at school or work. To my friends Alex de Lima and Raquel Simon, who were there through everything and keep being there through it all. To my stepfather, David Garcia, that gave me the opportunity to know what the word father is. To my teachers, my family, my friends, my nannies, my department committee, and Dr. Yuanbing Mao for all the support during these years.

ACKNOWLEDGEMENTS

The author thanks the financial support by the National Science Foundation under CHE (award #1710160) and DMR (grant #1523577) and the USDA National Institute of Food and Agriculture (award #2015-38422-24059, for the Integrating Food Science/Engineering and Education Network (IFSEEN) program). The University of Texas Rio Grande Valley for the generous support provided by a Departmental Grant from the Robert A. Welch Foundation (Grant No. BX-0048). Dr. Yuanbing Mao, Dr. Karen Lozano, and Dr. Mohammed Jasim Uddin for providing these grants for me to continue my education.

TABLE OF CONTENTS

Page

LIST OF TABLES

Page

LIST OF FIGURES

Page

CHAPTER I

INTRODUCTION TO NANOTECHNOLOGY

1.1.1 What is nanotechnology

Nanomaterials are known to be the manufacture development materials giving rise to potential properties covering the range of 1-100 nm.[1] Nanomaterials have increased a lot of research attention in the past years due to their unique size. The size in these materials develops many physical and chemical properties such as phase transition, theoretical strength, luminescence, electrical conductivity, etc. that are prone to quantum effects on atoms, molecule, and structure that may differ from those of bulk size materials. Such distinction in bulk and nanoscale materials ascends primarily due to an improved surface area considering that nanomaterials have a larger surface-area to volume ratio at nanoscale, the intrinsic properties are predominantly determined by size, atom composition, morphology, and crystallinity enhancing chemical reactivity and much improved mechanical strength than bulk materials.[2] Many scientists have manufacture controllable synthesis of size and shape at nanoscale having optimized pH, defect concentration, crystallinity, surface area for many fields such as medical, magnetics, energy, engine production, agriculture, optics, and more. (Figure 1.1) [3]

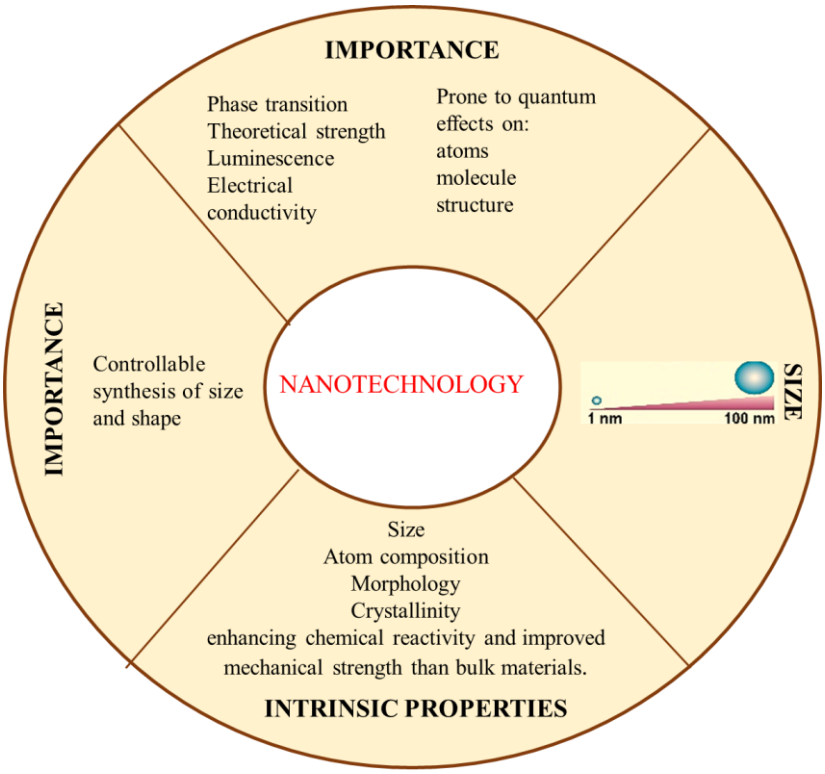

Figure 1.1: Scope to Nanotechnology

1.1.2 Importance of Nanoparticles

Nanoparticles are important from centuries ago before we knew these materials even existed in science. In the past, there were discoveries that Chinese heritage used to custom nanoparticles as an inorganic dye, Romans used metal nanoparticles to create glass objects, and now scientists used nanoparticles for science developments.[4] Nanoparticles are important now because is the main role in nanomaterials for scientist's ability to see and manipulate matter on a nanoscale based and try to understand an atomic scale interaction that still is far from science to be completely understood. [5]

Benefits and application of nanomaterials help expand, even transfigure science; for example, medical nanotechnology uses drug delivery in the human body by effective approaches to target nanoparticles carrying therapeutic drugs straight to ailing cells.[6] Diagnostic techniques are now using antibodies attached to carbon nanotubes to detect cancerous cells.[7] Antibacterial treatments aim to help destroy bacteria by the usage of gold nanoparticles and infrared light.[8, 9] Nanomaterials in optics focus in the performance and properties of light, including its interactions with matter and in the manufacture of instruments to detect the light been produced. [10]

Optical materials are proficiently used in optoelectronic, optic lasers as well as in LEDs light, solar energy and medical imaging. Such materials and the devices used in optical materials cover different spectra range such as UV, VIS, and IR.[9, 11, 12] Nanoparticle also play a role in superconductivity; scientist study the electron-photon interaction where atoms in a lattice are in constant vibration creating waves between these atoms, further creating these electron-photon interactions causing conduction.[13, 14] Some of the fields where superconductors and nanotechnology are used are gas storage, ultra-capacitors, batteries, flat-panel displays, etc. [15-17] Not only do nanoparticles play a role in medical science, physics, material science, but food.

Nanomaterials also obtained lot of research in agriculture using nano sensors, and nano catalysts; nano sensors are used to detect pesticides, contaminants, such as pathogens or allergens in food harvests.[18, 19] Nano catalyst are used for agricultural waste bioprocesses.[20] For these and many more fields in nanomaterials nanoparticles are a huge role in the development of nanoscience. (Figure 1.2)

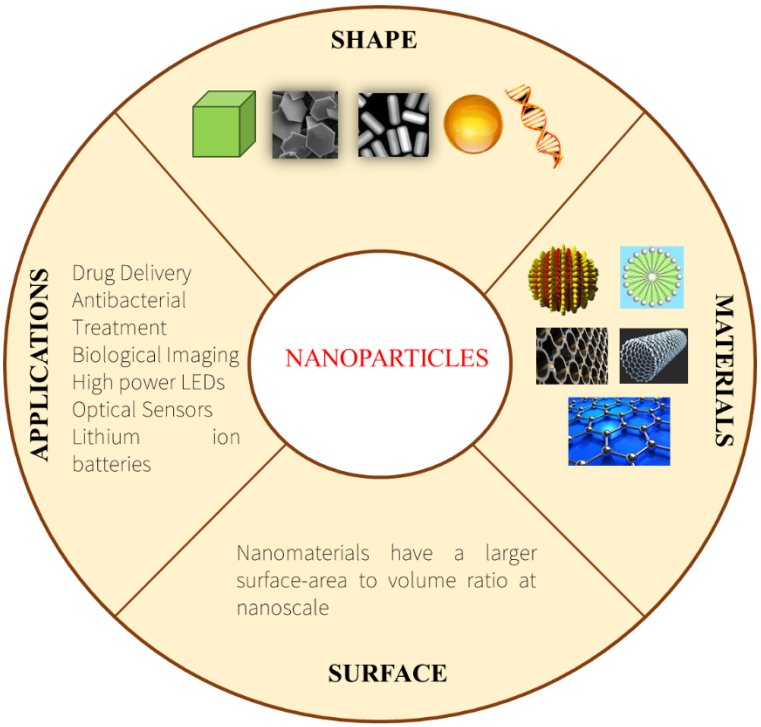

Figure 1.2: Scope to Nanoparticles

1.1.3 Nanoparticles by Molten Salt Synthesis

Molten salt synthesis (MSS) has been introduce to the world of nanotechnology as one of the simplest, environmentally friendly, low cost productions, and as an astonishing controllable medium to synthesize nanoparticles. [21-23]

The way molten salt synthesis works is by mixing the reactants by choice with a specific ratio of salts such as $NaNO_3$, KNO_3, NaCl, KCl, LiCl, $LiNO_3$, etc. The second process is the most important in molten salt synthesis since it involves the diffusion, disassociation, arrangements of the atoms by heating the mixture chosen with the molten salt; then the molten salt will behave as the medium for the reactants. The final step will deal with the growth and shape of nanoparticles by nucleation following Ostwald ripening mechanism. [24-26]

Molten salt synthesis investigations had concluded that molten salt has many advantages when it comes to use; such as; upturn the rate of chemical reactions, upturn the degree of reactant producing uniform, homogenous particles, as well as controlling crystalline size, morphology, and reduction of agglomeration between nanoparticles.[27] Molten salt synthesis simplicity has led many scientists to use this technique to develop metal lanthanides crystal structures with different chemical conformations such as perovskites (ABO_3), spinel (AB_2O_4), pyrochlore ($A_2B_2O_7$) and orthorhombic structures ($A_2B_4O_9$) in different fields such as scintillators, ceramics, thermal barrier coatings, luminescence, host radiation waste, etc. [28]

1.1.4 Importance of $A_2B_2O_7$ Host

Research based on $A_2B_2O_7$ structures obtained many research developments because the structure of these materials can be synthesized into two phase transitions; ordered pyrochlore and disorder fluorite; resulting in many different applications were these two phases can be useful. The formation of $A_2B_2O_7$ consisted of the A-site corresponds to a rare earth element with a charge of A^{3+}. The B-site corresponds to a metal transition element with a charge of B^{4+}. The difference between these two phases is on how the oxygens are arrange on the structure. (Figure 1.3) In ordered pyrochlore the oxygens are arrange on specific sites in the lattice making the structure more prone to have the following properties: high chemical stability, immobilization of high-level nuclear waste, wide band gap, luminescence properties, and ion conductivity etc.[29-32] Ordered pyrochlore due to these properties became suitable for applications such as host radiation waste, batteries, optic materials, catalysts, fusion reactors materials and more. In disorder fluorite, the oxygens follow a different arrangement by arranging randomly thru the

lattice causing this phase transition to develop properties such as phosphor materials, and high melting point use in applications such as ceramics and thermal barrier coatings. [33, 34]

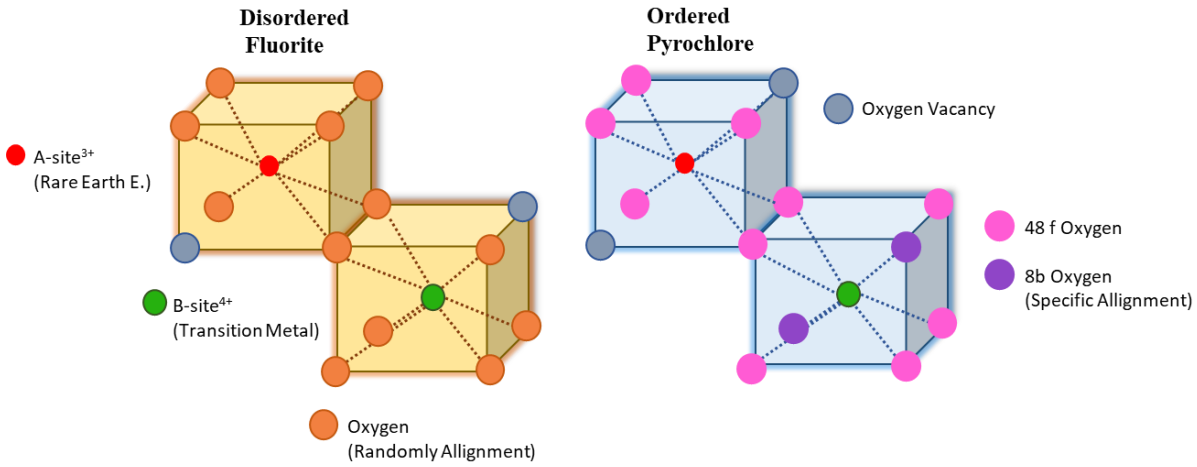

Figure 1.3: $A_2B_2O_7$ Phase Geometry

These two phases can accommodate the dopant elements and rare earth elements into both A and B-sites. Pyrochlore materials now a days are use more in the science field because the structure is more ordered, has a D_{3d} symmetry causing the cations to arrange in the most suitable way depending on the ion size leading to a more occupied lattice.[35] There are many $A_2B_2O_7$ structures been used to try to understand the many properties these materials can develop. In this work, $A_2B_2O_7$ structures will be only cover the structure $La_2Zr_2O_7$ ordered pyrochlore and its findings throughout two years of research data and analysis.

Rare earth zirconate pyrochlore constituents are broadly studied as an optical host and disorder to ordered phase transition by developing lanthanide-doped materials for various types of lanthanide ion such as Er^{3+}, Eu^{3+}, Dy^{3+}, Yb^{3+} etc. use directly towards phosphor applications.

[9, 36, 37] These phosphor materials have industrialized promising properties such as low phonon energy, high structural and thermal stability, due to higher electron-hole overlay that may yield high oscillator strength which can increase photo and radioluminescence efficacy. As for the reasonable size of La^{3+} ions, $La_2Zr_2O_7$ displays a fully ordered pyrochlore-type assembly with a space group of Fd-3m, also offering significant properties including, low thermal conductivity, and good ability to accommodate defects. [38, 39] $La_2Zr_2O_7$ has been extensively studied as a luminescence host however, none of past works focused on exploring doped lanthanum zirconate nanoparticles that will be beneficial for medical, scintillation and optoelectronic application.[40] Molten salt synthesis technique method has been achieved as one of the most effective and suitable method to synthesize $La_2Zr_2O_7$ because it requires as previous explained low cost, low input time, low temperature synthesis, and the synthesis can be controllable to develop suitable desire nanoparticles with well-organized properties. [41]

1.1.5 What is Upconversion

Upconversion (UC) is the system in which the absorption of two or more photons leads to the emission of light at a shorter wavelength than the excitation wavelength.[9] In other words; up-conversion deals with the activator (such as Ho, Er, Tm, $NaYF_4$) been in an intermediate state instead to be site in its ground state; this state will mark the interaction between a sensitizer (Such as Yb, Ce) and the activator to be lesser than the vibrionic interaction of both materials so that both can fuse into a single-ion level coupled to the crystal lattice of a compound.[42] Up-conversion progression is achieved throughout numerous mechanisms such as ground state absorption followed by excited-state absorption, sequential energy transfer, and photon

avalanche. Upconversion deals with anti-stoke lines; the difference of energy of the emitted photon which has more energy than the absorbed photon in a system. [43]

Upconversion is mostly use as the conversion of electromagnetic radiation with longer wavelengths (infrared light) to electromagnetic radiation that can be perceived by the human eye (visible light). In recent years, some of advantages of upconversion are attributed by having large anti-Stokes shifts, sharp-band emissions, long emission lifetimes, excellent photo stabilities, high light-penetration depth and low toxicity. Due to these characteristics up-conversion applications are optical features use in displays, laser and optical amplifiers, solar cells, biotechnologies, drug-delivery, biosensor, optical temperature sensors, and more. [44, 45]

1.1.6 What is Downconversion

Downconversion (DC) consist in one high energy photon dealing with thermalization; process in which elements reach thermal equilibrium by joint interactions which in this case is inadequately absorbed due to thermalization losses by a system, which then is transmuted into two or more lower energy photons. Down-conversion is mostly use as the conversion of electromagnetic radiation with a wavelength size from 10 to 400 nm (ultraviolet light) to visible light. [46, 47]

Downconversion materials exclusive physiognomies arise from the presence of narrow band gaps which makes the process suitable for application such as, solar cells, luminescence devices, optical transmission, medical diagnostics, biochemical probes, etc.[48]

1.1.7 Uses in Luminescence Materials

Luminescence is the transition of an atom from the excited energy state to a lower energy state and then releasing quantum energy in the form of a photon of the system. Nanoparticles are suitable in optical materials due to size-dependent physical and chemical characteristics. The sizes in nanoparticles incline to have a large surface area in comparison with their volume making nanoparticle very volatile to many applications. Nanoparticles tend to emit light or glow with a light frequency depending on the material composition use and particle sizes gain after synthesis method making them suitable for luminescence materials. [49, 50]

In $A_2B_2O_7$ host materials, the area of interest in luminescence characteristics tend to be infrared region, cathodoluminescence, efficient pump-power dependence, energy transitions, lifetime, quantum yield, radio-luminescence etc. [51-53] In pyrochlore host materials since the A-site deals with lanthanide elements, the optical properties of these materials tend to be originated from electron configurations of 4f transitions of such elements. In luminescence materials there are various factors to consider when studied. Photoluminescence tends to be affected by size and structure by changes in synthesis, time, temperature, pH, etc. so controllable factors are required for scientist to obtained better annotations in growth mechanism, energy transitions, luminescence lifetime, and morphology.

1.1.8 Dopant Role in $A_2B_2O_7$ Host

A dopant material is a trace of impurity element that is incorporated into a chemical compound or if it is crystalline material it will be incorporated into the crystal lattice to stimulate emission and modify its original optical and electrical characteristics. Doped materials obtained intense scientific work in the areas of lighting, LEDs devices, bioimaging, display materials, and thermometry. Rare-earth doped materials are known for their elevated luminescence quantum yield and chemical stability due to the f-f forbidden transitions and f-d transitions of these elements suitable for optical devices. Pyrochlore structures tend to be an exceptional host for rare earth dopant materials in recent years.[54] In this work, the use of Europium (Eu) as a dopant element is under down-conversion studies with Lanthanum zirconate due to strong luminescence and radiation stability in nanocrystal structures. Eu tends to give effective and rapid luminescence due to allowed 5d-4f transitions of Eu^{3+} causing intense values and lower thermal conductivity when combine with lanthanum zirconate. Eu can serve as a substitute phosphor active element in the host lattice by assessing local site symmetry with a nondegenerate state that cause no splits by crystal field effects.[12, 55]

In upconversion materials, the introduction of Gd, Yb, Tm, and Er as dopants offer ultraviolet upconversion (UVUC) emissions for the manufacture of UV devices. Moreover, $A_2B_2O_7$ host materials have been study by using triply doped materials (Gd, Yb, Tm) for NIR excitation to UVUC emission. Dopant such as Yb^{3+}-Er^{3+} conjunction expands absorption cross-section of 980 nm photons because Yb^{3+} ions stimulate Er^{3+} ions to greater energy levels through energy transfer.[30, 56] Er^{3+} characteristics show an extensive narrow linewidth in

addition to a high degree of wavelength stability. Tm^{3+} has fitting stable state levels for UVUC emission through the single transition of $^2F_{7/2} \rightarrow {}^2F_{5/2}$. The ultraviolet to visible absorbance spectra, Gd^{3+} as a dopant displays a blue shift by increasing Gd dopant concentration. Similarly, as Gd^{3+} concentration increases so does the band gap of the system. The photoluminescence spectra of Gd^{3+} doped materials also display a green increase of intensity as Gd^{3+} incorporated into the crystal lattice by oxygen vacancies occurring. Dopant elements had help rare earth elements display many attributions to science. In this work, dopant elements play a huge role in photoluminescence and how factors such as temperature, time, dopant selection affects the host lattice and its characteristics.[57, 58]

CHAPTER II

METHOD SYNTHESIS TO ACHIEVE $A_2B_2O_7$ NANOMATERIALS

2.1.1 Materials

Sodium nitrate Reagent Plus ($NaNO_3$, 99.0%), Erbium nitrate pentahydrate ($Er(NO_3)_3 \cdot 5H_2O$, 99.0%), Potassium nitrate Reagent Plus (KNO_3, 99.0%), Ytterbium nitrate pentahydrate ($Yb(NO_3)_3 \cdot 5H_2O$, 99.0%), Sodium chloride BIOXtra (NaCl, 99.5%), Thulium nitrate pentahydrate ($Tm(NO_3)_3 \cdot 5H_2O$, 99.0%), Potassium Chloride BIOXtra (KCl, 99.0%), Europium (III) nitrate hexahydrate ($Eu(NO_3)_3 \cdot 6H_2O$, 99.9%), Zirconium(IV) oxynitrate hydrate ($ZrO(NO_3)_2 \cdot xH_2O$, 99.99%), Lanthanum(III) nitrate hexahydrate Reacton ($La(NO_3)_3 \cdot 6H_2O$, 99.99%), Ammonium hydroxide (NH_4OH, 28%), and Gadolinium nitrate pentahydrate ($Gd(NO_3)_3 \cdot 5H_2O$, 99.0%), were acquired from Alfa Aesar Company and Sigma-Aldrich Company. [59, 60]

2.1.2 Experimental Synthesis

Co-Precipitation Method

Lanthanum (III) nitrate hexahydrate and Zirconium (IV) oxynitrate hydrate and dopant element Eu (5%), Tm (1%), Er (3%), Gd (20%), Yb (0.25%-20%) with a 5:5 ratio were dissolve into a beaker with 200 ml of deionized water for 30 min. under stirring condition. In another beaker a solution of 180 ml of deionized water and 20ml of Ammonium hydroxide were mixed and then transfer by driblets via titration for 2 hours to the mixture under stirring condition to

create a white precipitate. The precipitate was let to settle overnight before washing. The precipitate was washed several times until neutral pH of 7.0 is reached. After that, the white precipitate was collected via vacuum-filtration and let dried at room temperature for two days. [31]

Molten Salt Synthesis (MSS)

A molten salt combination was synthesize by initially mixing the sodium and potassium nitrates with the formed single-source precursor in a ratio of 30:30:1 by grinding, then heated in an alumina crucible by a muffle furnace at 650°C for 6 hours with ramp-up and -down rates of 3°C/min, and finally washed with DI water multiple times to remove the salts to form "LZOD-P NPs" (D, represent the dopant element use) For down-conversion data explanation, the dopant use was exclusively Eu. For up-conversion data explanation, the dopant use was Tm, Er, Gd, and Yb.

To explore the effects of molten-salt dispensation on the structure, particle size, and optical properties of these preformed LZOE-P NPs on down-conversion, a mixture of NPs with sodium and potassium nitrates or chlorides in a molar ratio of 1:30:30 was study under different processing times (3h, 6h, 12h, and 24h) and annealing temperatures (i.e. 650°C, 800°C, 950°C, and 1100°C) with ramp-up and down rates of 3°C /min. The obtained products after washed and purified with deionized water were designated on the format of LZOE-t (the number of processing hours)-T(the number of processing temperature)-molten-salt medium (shorted as N and C for the nitrate and chloride salts, respectively). The representation of molten-salt processing for upconversion and down-conversion LZOD-P NPs is showed in (Figure 2.1) [59]

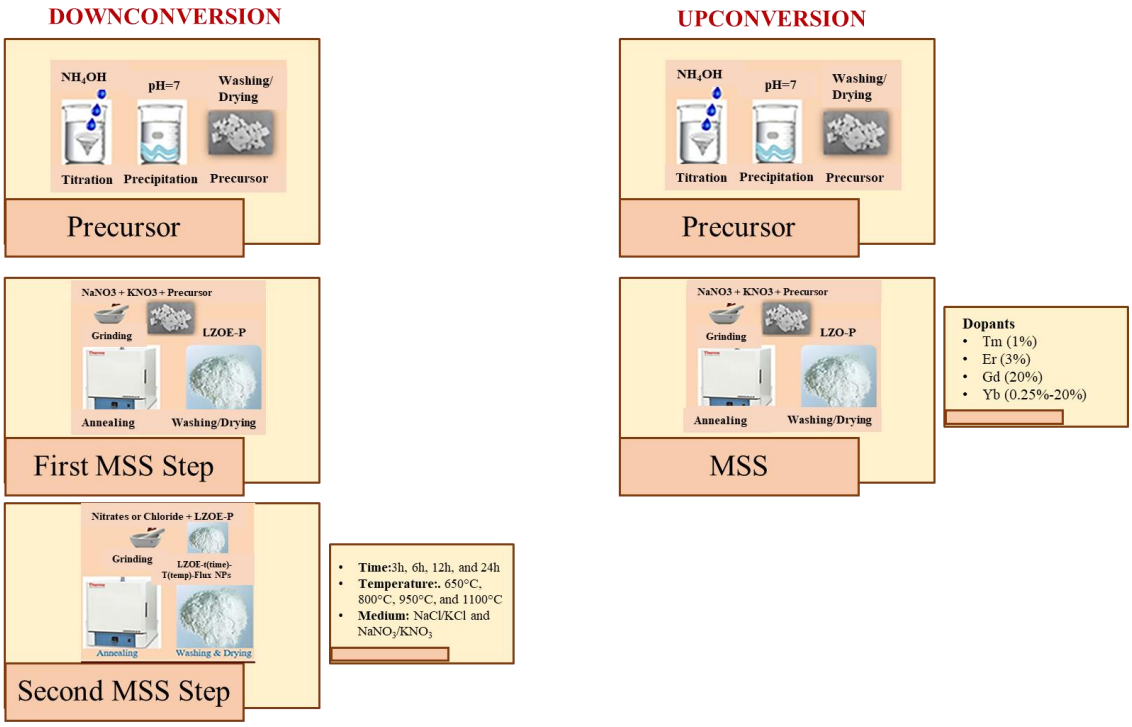

Figure 2.1: Molten Salt Synthesis for $A_2B_2O_7$ Structures

2.1.3 Different Method Types to synthesize $A_2B_2O_7$ Nanomaterials

Nanoparticles can be synthesized by a variety of different techniques to achieve the range of 1-100 nm. There are different methods with different characteristics use depending on the shape, geometry or form researchers will like to achieve in the most efficacy way. In this work, the methods explain are hydrothermal synthesis, co-precipitation, and Sol-gel synthesis. [32, 61]

Hydrothermal Approach

Hydrothermal consist in performing a chemical reaction of reactants in aqueous solution under a closed compartment, where the heated aqueous solution will surpass ambient pressure and temperature conditions in the system. Hydrothermal is performed for the preparation of inorganic-organic materials, crystals, complex oxides, luminescence phosphors and nanomaterials.

The method consists in the mixture of the reactants desire with water or a solvent such as ethanol, ammonia to cause a precipitation to be pour into a steel pressure device called autoclave, then the mixture is now heated to a specific low temperature for a controllable duration time causing the water or solvent to dissolve, precipitate the reactants and growth of the system wanting to be achieved. Some of the advantages of using hydrothermal as a method are; easy and precise control of size, morphology, and crystallinity by the modification of time and temperature in the closed compartment. (Figure 2.2)

Huge improvement in the chemical activity of the compound been synthesized. Also, hydrothermal is use as a soluble mechanism for reactants in hydrothermal when match with a correct solvent to reach a critical point in the reaction. Some of the disadvantages in hydrothermal approach are; the expensive steel close compartment cost needed, contamination during reaction if compartment is not close properly, high temperatures can damage the vessel inside of the autoclave causing to be melted and the synthesis expose to malformation or no production of the material desire. [62, 63]

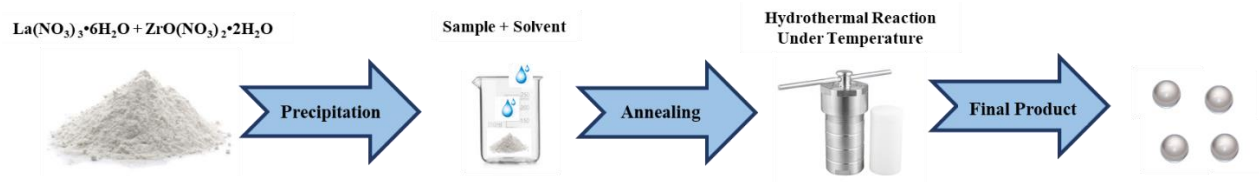

Figure 2.2: Hydrothermal Synthesis

Co-precipitation Approach

Co-precipitation is use for synthesizing high-purity materials under low annealing temperatures. Co-precipitation involves the manufacture of a precursor with nitrates to chlorides which then is mixed and precipitated by the use of a solvent to stimulates the growth and nucleation in a system. Some of the advantages that co-precipitation provides are; the facilitation to produce insoluble materials by supersaturation, nucleation is an important role in the formation of nanoparticles for $A_2B_2O_7$ materials, reactants can be controllable synthesize by controlling different factors like solvent concentration, titration time, temperature, etc. Just like any technique co-precipitation contain disadvantages such as impurities may precipitate as well with the reactants, long time process, resynthesized may not have the same results as the first synthesis affecting control in the experiment. (Figure 2.3) [64, 65]

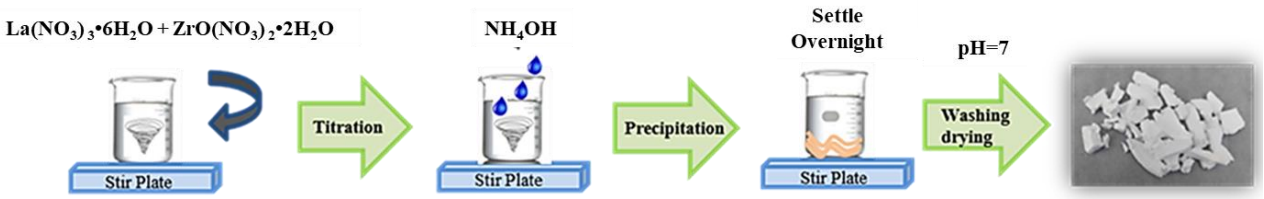

Figure 2.3: Co-precipitation Synthesis

Sol-gel Approach

Sol-gel is the technique where hydrolysis and polycondensation is needed for the formation of a reactant mixture with an aqueous solution where different factors such as chemical reaction, temperature, gelation causes the solution to arrange itself into a gel foundation. This gel helps avoid segregation between the particles at low temperatures when the synthesis is in process. Some of the advantages of sol-gel are; low temperature synthesis, purity increase in compounds synthesize under sol-gel, successfully mixture of reactants in liquid form, control of dopant dispersion in synthesis. Sol gel also has some disadvantages such as solvents may cause harmful human damage, and long engage time during synthesis. (Figure 2.4) [47, 66]

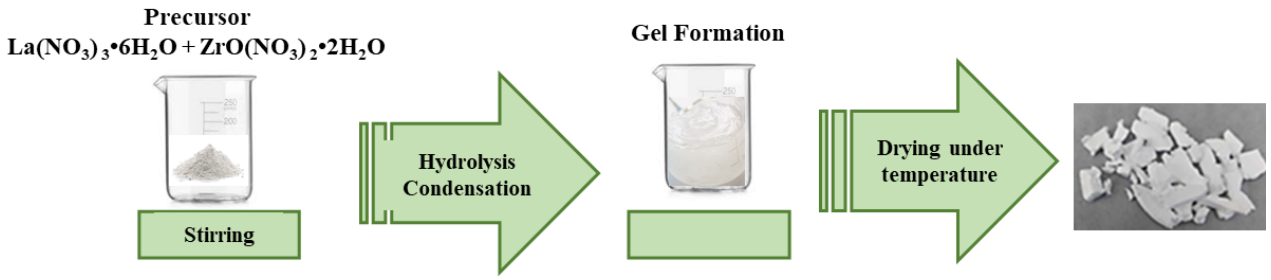

Figure 2.4: Sol-gel Synthesis

CHAPTER III

CHARACTERIZATION

3.1.1 X-Ray Diffraction

X-ray diffraction is defined as an analytical technique which allow scientists to acquire information regarding phase identification of a lattice and its cell dimensions. X-ray diffraction take place when a scattered beam of a monochromatic x-ray penetrates the target compound. The scattered light experience constructive (waves in phase) and destructive (waves out-of-phase) interference.[67, 68] X-ray diffraction mechanism consists for the x-ray light to rotate around the targeting material placed in a stage, where only if the radiation waves became in phase with the sample; will result in a specific diffraction peak at a specific angle providing bond lengths, bond angles, and the virtual sites of ions and molecules in the unit cell. In nanomaterials, crystalline structures are very common resulting in the usage of x-rays by crystals described by Bragg's equation.

$$2d\sin\theta = n\lambda$$

Where d is the distance from two parallel planes of atoms by the scattering light. The n is an integer and wavelength (λ) which is the specific angle where the radiation waves became in phase causing a diffraction peak. There are factors which cause the direction of the diffraction dependent such as size, shape, and intensities of the lattice giving scientist an insight of properties

in the unit cell. Nanoparticles produce via molten salt synthesis results in powder samples where the Debye-Scherer formula needs to be used to be able to determine crystallite size. [19, 65, 69]

$$D = \frac{K\lambda}{\beta \cos\theta}$$

where D signifies the crystallite size, K is a constant of the Scherer formula with a value of 0.94 for cubic crystallites. X-ray wavelength (λ) spectroscopy provided by the institution has a value of 1.5406 Å, β is the full width half-maximum (FWHM) of the highest peak in the sample; for $A_2B_2O_7$ materials the highest peak corresponds to the (222) peak of the nanoparticles minus the FWHM fitting of the instrument, and θ is the angle of the corresponding Bragg reflection fitted in accordance with the calculate FWHM of the (222) peak. For data collection, x-ray diffraction was elemental for crystallite size and phase transition from disorder fluorite to ordered pyrochlore.

3.1.2 Scanning Electron Microscopy

Scanning electron microscope is very helpful in science to observe morphology, particle size, and physical topographies on a lattice area; where the simple eye is unable to determine the characteristics in question. Scanning electron microscope is able to display images where scientists are able to note changes in size and morphology by different parameters employ in the sample been study. The electron scattering and sample interaction creates several motions that result in an image. Scanning electron microscope uses an electron foundation, where electrons are produced and release through a column where a variety of electrons are dispersed over a sample. Scanning electron microscope uses electromagnetic lenses as a controllable way for electrons to follow the column pathway; enhancing good quality images. The condenser controls the

resolution on the electron beam, while objective lenses are operated to focus the beam into the sample. Magnification will depend on the abilities of the machine use and on the size of the particles gained. [70]

3.1.3 Raman Spectroscopy

Raman spectroscopy is an advantageous technique to study molecular vibration in a structure and it has the unique ability to offer a structural fingerprint by which molecules can be acknowledged. Raman spectroscopy follows the Raman effect; when a monochromatic light hits a sample, some light will be scattered, and some will be absorbed by the sample. Then a certain part of the energy gets transmitted to the sample by Raman scattering. When studying $A_2B_2O_7$ phase arrangement, Raman spectroscopy is one of the most wanted techniques to identify between disorder fluorite (DF) or ordered-pyrochlore (OP) lattice structure. The way to contrast between these phases is that a DF structure with space group $Fm\bar{3}m$ only has one Raman active mode assigned to F_{2g} and will be identify in the spectra by a broad peak covering the range categorize by a DF phase. DF mode is principally accredited to random positioning of seven O^{2-} ions over eight anionic sites in the lattice leading to high level of structural disordering. In contrast, the OP structure is defined with $Fd\bar{3}m$ space group holding six Raman modes ($A_{1g} + E_g + {}^4F_{2g}$) that occur in the range of 200 cm^{-1} to 1000 cm^{-1}. The modes are principally accredited to specific molecular vibrations between O^{2-} ions and the A and B-site will result in specific peaks located throughout the spectra. [25, 45, 55, 56]

3.1.4 Optical Spectroscopy

Photoluminescence (PL) measures the intensity of light released from the excited state to ground state of a sample when irradiated by a monochromatic light over a spectrum of wavelengths. By determining the luminescence spectrum, it is likely to observe material imperfections and impurities. In this work, study the luminescence of materials, which involves the metal oxide elements (host) and rare earth ions (activator) in the valance state is fundamental. To study photoluminescence, a background study of the luminescence phenomenon needs to be done, then representations are recorded linked with the energy levels of the ground state where it will construct a relationship between the host and activator been used. [31, 71, 72]

3.1.5 Characterization use for experimental purposes

The spectroscopy techniques used for $A_2B_2O_7$ nanoparticle materials by molten-salt processing exposed once or twice were characterized using X-ray diffraction (XRD), Raman spectroscopy, scanning electron microscopy (SEM), photoluminescence spectroscopy (PL) and lifetime decay, and. XRD patterns were taken by Benchtop powder X-ray Rigaku-Miniflex diffractometer having a Cu Kα1 radiation (λ = 0.15406 nm, 115V, 50/60 Hz) with a scanning 2θ range of 20-90º, step size of 0.05º and rate of 1.12º/sec. Raman spectra were taken by a Senterra Bruker spectroscope (OPUS 7.5 Software) with a 785 nm laser and 50 mW at a resolution of 3-5 cm-1 and integration time of 10 second. SEM images were collected using a Carl Zeiss Sigma-VP field emission SEM. Fiji image analysis software using ImageJ 64bit as the system to develop histograms and particle size distribution for SEM images. PL spectrum were recorded using an Edinburgh Instrument FLS 980 fluorometer with a xenon lamp. Lifetime decay profiles

were collected on the FLS 980 fluorometer by implementing a pulsed microsecond xenon lamp with a frequency from 1-100 Hz using time correlation with single-photon counting method.[59]

CHAPTER IV

DISCUSSION

4.1.1 X-Ray Diffraction Analysis

Downconversion

For the simplicity of discussion, the molten-salt processing time, temperature, and type of salts will be explained consecutive with each spectroscopy technique to compare the different results obtained in preformed LZOE NPs when exposed to different factors.

Molten-salt processing time

X-ray diffraction was performed in LZOE NPs to confirmed purity by noting no additional peaks in the spectra. XRD patterns of the preformed LZOE NPs and molten-salt processing with a control temperature of 800°C, chloride salts as the medium and different processing times (Figure 4.1a) show pure phase matched with the standard XRD pattern of LZO (JCPDS card No 71–2363). After using Debye-Scherer formula explained in chapter III, the computed crystallite size of the LZOE NPs (Table 1) visibly sight the crystallite size increasing from 22 nm to 29 nm as the molten-salt processing times increase from 0h to 24h. [27]

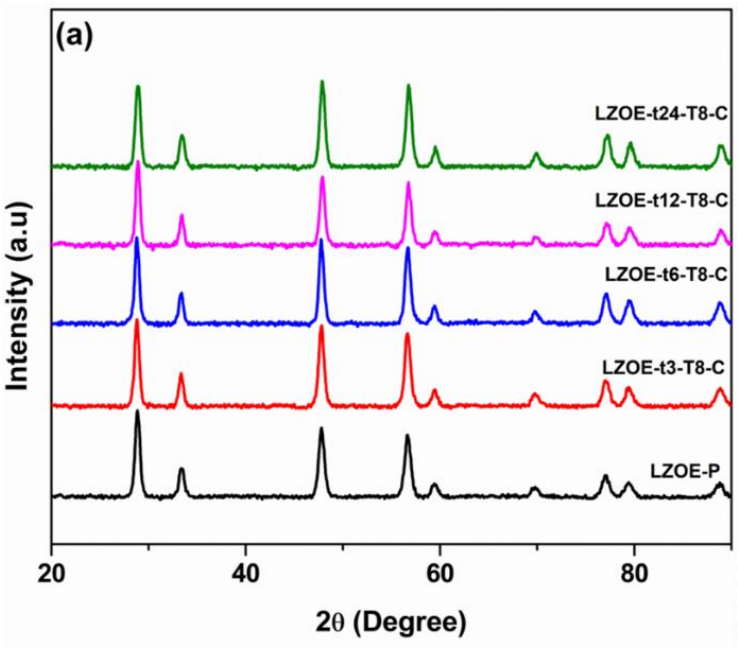

Figure 4.1 (a) XRD patterns of the preformed LZOE NPs with a control temperature processed at 800ºC in mixed sodium and potassium chloride medium with different molten-salt processing times.

	LZOE-P	LZOE-t3-T8C	LZOE-t6-T8C	LZOE-t12-T8-C	LZOE-t24-T8-C
2θ (º) of (222) peak	28.85	28.8	28.75	28.9	28.8
FWHM (β) of (222) peak	0.5742	0.5382	0.52397	0.50596	0.4874
Calculated crystallite size from XRD (nm)	22	24	25	27	29
Calculated lattice parameter (Å)	10.71	10.73	10.75	10.69	10.73
FWHM of Raman F_{2g} peak	326.43	503.609	534.46	535.99	519.34
Estimated particle size from SEM (nm)	32.4 ± 0.4	33.3 ± 0.4	37.4 ± 0.4	45.9 ± 0.8	47.5 ± 0.8
PL lifetime (ms)	1.76	1.77	1.65	1.84	1.95

Table 1. Changes of structural and optical parameters after the preformed LZOE NPs with a control temperature processed at 800ºC in mixed sodium and potassium chloride medium with different molten-salt processing times.

Molten-salt processing temperature

XRD Patterns exhibit in Figure 4.2a display the single-phase of LZOE NPs without any impurity and equivalent with JCPDS patterns 71-2363. It was noted that as temperature increases, sharper diffraction peaks appear connotating high crystallinity and increase in crystallite size of the LZOE NPs. After calculations, the crystallite size in Table 2 data shows an increase from 22 nm to 34 nm as the different variables in temperature (650ºC to 1100ºC) increases. There was a slightly difference where the changes in crystallite size was larger by the different processing temperatures used that the crystallite size by the different processing times used in this study. The increase in crystallite size is ascribed to Ostwald ripening which defines the modification of an inhomogeneous compound. In this case, the greater particles raise bigger at the expense of the slighter particles demonstrating the relationship LZOE NPs surface area to volume ratio (S/V). [73]

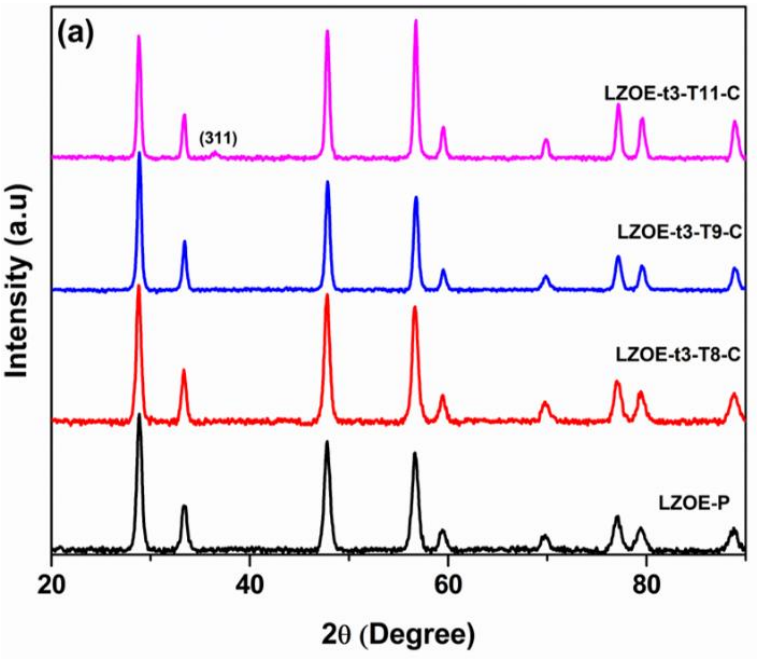

Figure 4.2 (a) XRD patterns of the preformed LZOE NPs with a control processed time at 3h in mixed sodium and potassium chloride medium with different molten-salt processing temperature

	LZOE-P	LZOE-t3-T8C	LZOE-t3-T9-C	LZOE-t11-C
2θ (º) of (222) peak	28.85	28.75	28.85	28.8
FWHM (β) of (222) peak	0.5742	0.5239	0.4454	0.43977
Calculated crystallite size (nm)	22	25	33	34
Calculated lattice parameter (Å)	10.71	10.75	10.71	10.73
FWHM of Raman F_{2g} peak	326.43	503.60	537.88	494.57
Estimated particle size from SEM (nm)	32.4 $\pm$ 0.4	33.3 $\pm$ 0.4	40.9 $\pm$ 0.5	49.7 $\pm$ 0.6
PL lifetime (ms)	1.76	1.77	2.16	1.99

Table 2. Changes in structural and optical parameters after molten-salt processing of the preformed LZOE NPs with a control processed time at 3h in mixed sodium and potassium chloride medium with different molten-salt processing temperatures.

Molten-salt processing Medium

In this section, LZOE NPs was formed by two different molten-salt mediums; for purpose of the study, the molten-salt processing temperature and time has been controlled for data processing. The following preformed samples were compared with LZOE-P NPs. The first medium $NaNO_3$-KNO_3 (at 650ºC for 6h) and the second medium NaCl-KCl (at 1100ºC for 6h) show XRD patterns (Figure 4.3a) effortlessly matched the characteristic diffraction peaks of $La_2Zr_2O_7$ in accordance with already explained JCPDS patterns. Table 3 data show the estimated before and after synthesis cell parameters and crystallite sizes of LZOE NPs after different molten-salt types. [74]

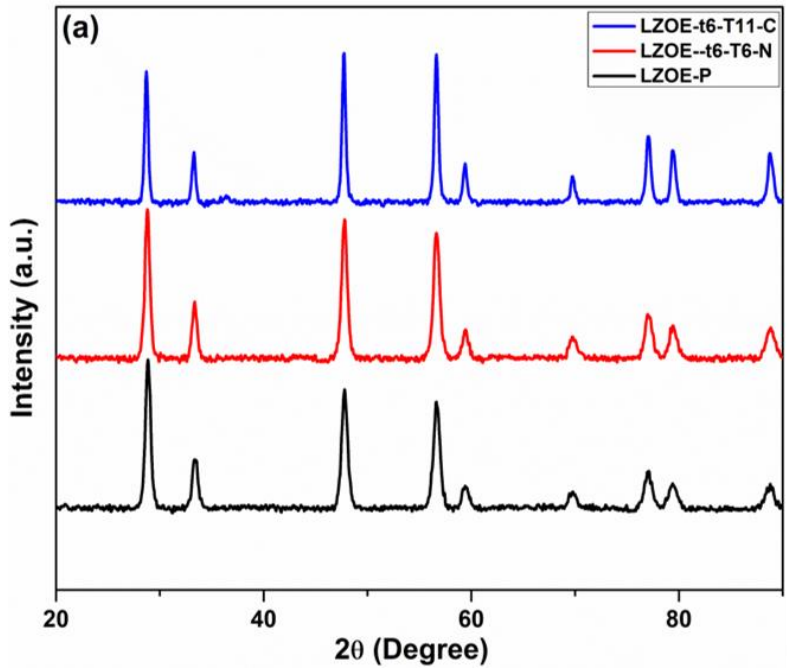

Figure 4.3 (a) XRD patterns of the preformed LZOE NPs after processed in the $NaNO_3$-KNO_3 and NaCl-KCl molten-salt media for 6h at 650^{o}C and 1100^{o}C.

	LZOE-P	LZOE-t6-T6-N	LZOE-t6-T11-C
2θ (º) of (222) peak	28.85	28.8	28.7
FWHM (β) of (222) peak	0.5742	0.5382	0.39227
Calculated crystallite size (nm)	22	24	42
Calculated lattice parameter (Å)	10.71	10.73	10.76
FWHM of Raman F_{2g} peak	326.43	534.46	505.54
Estimated particle size from SEM (nm)	32.4 $\pm$ 0.4	42.3 $\pm$ 0.6	59.3 $\pm$ 0.9
PL lifetime (ms)	1.76	1.65	1.99

Table 3. Changes in structural and optical parameters of the preformed LZOE NPs after processed in the $NaNO_3$-KNO_3 and NaCl-KCl molten-salt media for 6h at 650ºC and 1100ºC.

4.1.2 Scanning Electron Microscope Analysis

Molten-salt processing time

SEM data images including histogram insets in Figure 4.4 corresponding to particle size of LZOE NPs are shown. Molten-salt different process times compare with the before treatment of LZOE NPs shows particles with a spherical shape and constant progress of the average particle size from 32 nm to 48 nm. At different annealing times, solid-state materials crystalline to suitably high temperature enabling Oswald ripening. As previously explained, the greater particles raise bigger at the expense of the slighter particles showing the rate limiting factor to be diffuse oriented. Hence, increase in particle size normally follows exponentially with temperature, only linearly with the times chosen in the experiment and at a given controlled temperature like shown in the work. [75]

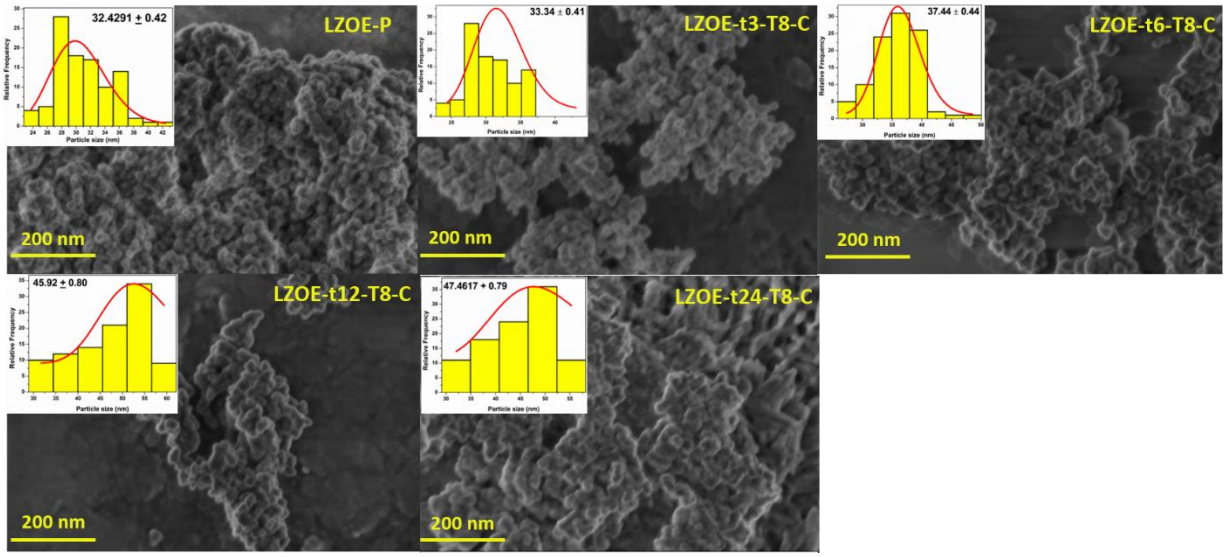

Figure 4.4. SEM images of the preformed LZOE NPs with a control temperature processed at 800ºC in mixed sodium and potassium chloride medium with different molten-salt processing times. The insets show the histograms of the particle size obtained from the ImageJ software.

Molten-salt processing temperature

SEM images (Figure 4.5) visibly displays preformed LZOE NPs with a sphere nanodomain morphology; as temperature progress an increase in aggregation happened. It is noted that as temperature increases, particle size enlarge from 33 nm to 50 nm (insets of Figure 4.5 and Table 2). The cause aggregation increases with temperature increase, is the self-assemble of the small particles into spheres of large masses. The spheres start creating masses around them, fussing into larger sized NPs. Yang et al. demonstrate this nanomaterial behavior where nanoparticles tend to self-assemble in different morphologies by mechanical properties originated by surface and strength of NPs adhesion.

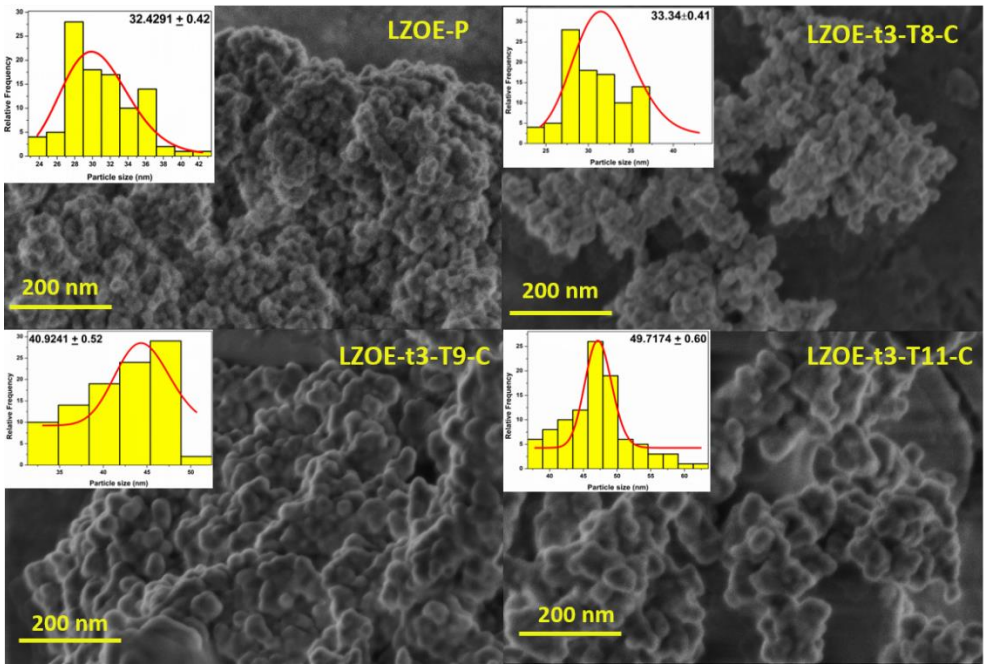

Figure 4.5 SEM images of the preformed LZOE NPs with a control processed time at 3h in mixed sodium and potassium chloride medium with different molten-salt processing temperatures. The insets show the histograms of the average particle size estimated using the ImageJ software.

Molten-salt processing medium

Nanoparticle formation in MSS is dictated by nucleation and crystal expansion process and the rate ratio defining particle size and morphology. In this case, a higher increase in the rate of nucleation, a higher grow of the particle size and the formation of a better well-define crystal shape. On the other hand, when crystal expansion rate is bigger than the nucleation, uniform nanoparticles are molded. The preformed LZOE NPs SEM images (Figure 4.6) and the after-process particles with different mediums show that larger particle sizes were obtained in the chloride medium. Data confirm nitrate medium (KNO_3-$NaNO_3$) at 6h/650ºC is about 42 nm and that of as-

synthesized sample in term of chloride medium (KCl-NaCl) at 6h/1100°C is approximately 59 nm.

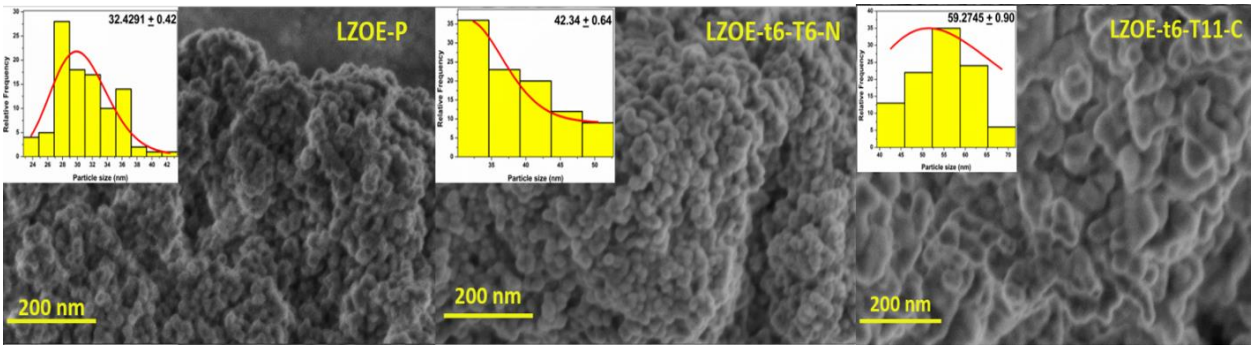

Figure 4.6 SEM images of the LZOE NPs after processed in the $NaNO_3$-KNO_3 and NaCl-KCl molten-salt media for 6h at 650°C and 1100°C. The insets show the histograms of the average particle size calculated using the ImageJ software.

4.1.3 Raman Spectroscopy Analysis

Molten-salt processing time

The Raman spectra of the preformed LZOE NPs with a control temperature at 800°C with different processing times (Figure 4.7) exhibit the Raman bands formation corresponding to the ordered pyrochlore structure. It is noted that as processing time increases, so does the broadening of the estimated FWHM (Table 1) The increase FWHM of the Raman F_{2g} band at ~300 cm^{-1} suggests enlarged anion disordering of the LZOE NPs with a control temperature at 800°C with different processing times compared with the preformed sample. [76, 77]

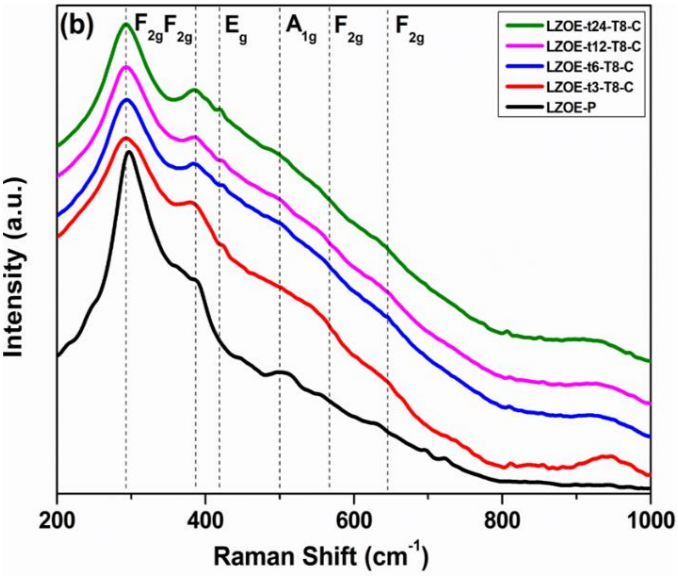

Figure 4.7 Raman spectra of the preformed LZOE NPs with a control temperature processed at 800ºC in mixed sodium and potassium chloride medium with different molten-salt processing times.

Molten-salt processing temperature

The Raman spectra (Figure 4.8) displays the Raman bands corresponding to OP structure for preformed LZOE NPs and after post synthesis with temperature as the variable and a control time of three hours under mixed sodium and potassium chloride molten-salt medium. (Table 2) calculations show the Raman bands to narrow as the processing temperature increases from 800 to 1100ºC proposing the ordering extend increase for OP structure to be reciprocal. In consequence, XRD and Raman results under molten-salt processing temperature express that particle growth of LZOE NPs and crystal lattice structure converts into higher degree of ordering as preformed LZOE NPS are synthesis to higher molten-salt processing temperatures under Ostwald ripening mechanism.

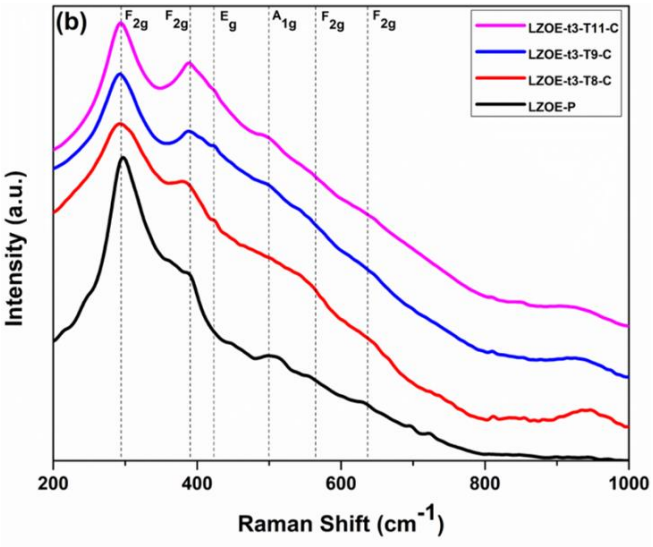

Figure 4.8 Raman spectra of the preformed LZOE NPs with a control processed time at 3h in mixed sodium and potassium chloride medium with different molten-salt processing temperatures.

Molten-salt processing Medium

Raman spectra data for different molten-salt processing mediums shows the same results explained before where the six Raman bands can be recognized in the spectra for OP structures. It is noted that there is a higher degree of intensity, ordering of oxygens, and slighter Raman bands in sample "LZOE-C" when compare with "LZOE-P" and "LZOE-N" samples (Table 3). The reason of the higher ordering and intensity in sample "LZOE-C" is due to higher temperature use in chloride molten salts synthesis resulting in higher Raman band definition.

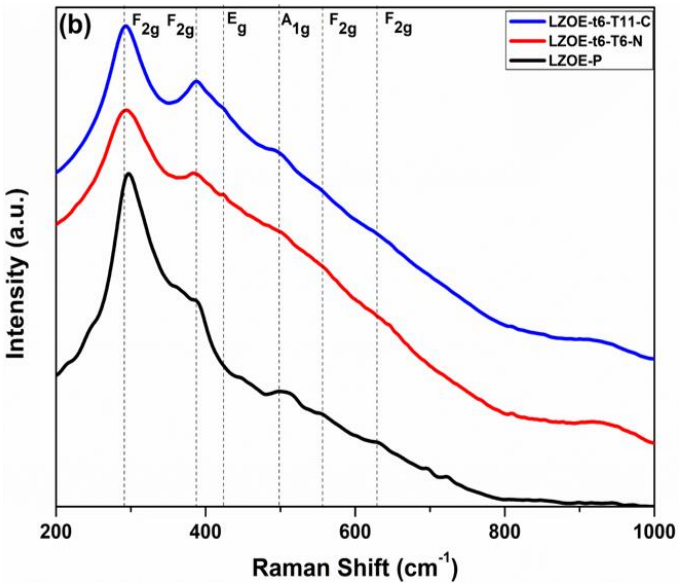

Figure 4.9 Raman spectra of the preformed LZOE NPs after processed in the $NaNO_3$-KNO_3 and NaCl-KCl molten-salt media for 6h at 650°C and 1100°C.

4.1.4 Optical Analysis

Molten-salt processing time

The emission spectra of the LZOE NPs was recorded to investigate luminescence behavior in each sample. LZOE NPs emission consist of strong bands of $^5D_0 \rightarrow {}^7F_1$ (592 nm), $^5D_0 \rightarrow {}^7F_2$ (612 nm), $^5D_0 \rightarrow {}^7F_3$ (653 nm) and $^5D_0 \rightarrow {}^7F_4$ (709 nm) once the charge transfer band was excited, (Figure 5a). At 592 nm; an orange emission is noted belonging to the magnetic dipole $^5D_0 \rightarrow {}^7F_1$ transition of Eu^{3+} which values do not change significant due to the crystal field strength. At ~612 nm; a red emission is noted to be related to the electric dipole $^5D_0 \rightarrow {}^7F_2$ transition of Eu^{3+} which the dependency on the symmetry of the crystal field makes Eu^{3+} very susceptible to the local environment around the element. Structural information about Eu^{3+} ions local symmetry is obtained when intensity ratios between $^5D_0 \rightarrow {}^7F_2$ to $^5D_0 \rightarrow {}^7F_1$ are compared

around LZOE NPs data. The asymmetry ratio $^5D_0 \rightarrow {}^7F_1$ line at 612 nm (ED) is stronger and higher in intensity in contrast to $^5D_0 \rightarrow {}^7F_1$ line at 592 nm (MD) which demonstrates that the asymmetric surroundings with no inversion symmetry was occupy by Eu^{3+} ions.

The excitation spectra in (Figure 5c) shows the charge transfer (CT) band from $O^{2-} \rightarrow Eu^{3+}$ ions which is identify as a broad band in the range of 250–360 nm and several lines in the range of 360–420 nm. Furthermore, the emission and excitation spectral data (Figures 5a and 5c) no profound change after different times were implemented unlike the intensity. The intensity difference as time increases (Figure 5b) shows in the preformed LZOE NPs have the highest emission value which then decrease after at 800°C in mixed sodium and potassium chloride medium for different time durations. The change in intensities after time increases is due to light scattering by particles agglomerating increasing particle growth with time exposure. The increase in agglomeration cause the scattering of emission and excited light to reduce in intensity after time exposure. When different molten-salt processed LZOE samples with different durations from 3h to 24h, 3h had the highest intensity due to high-quality properties since it had the least surface defects by higher crystallinity and least agglomeration. [78, 79]

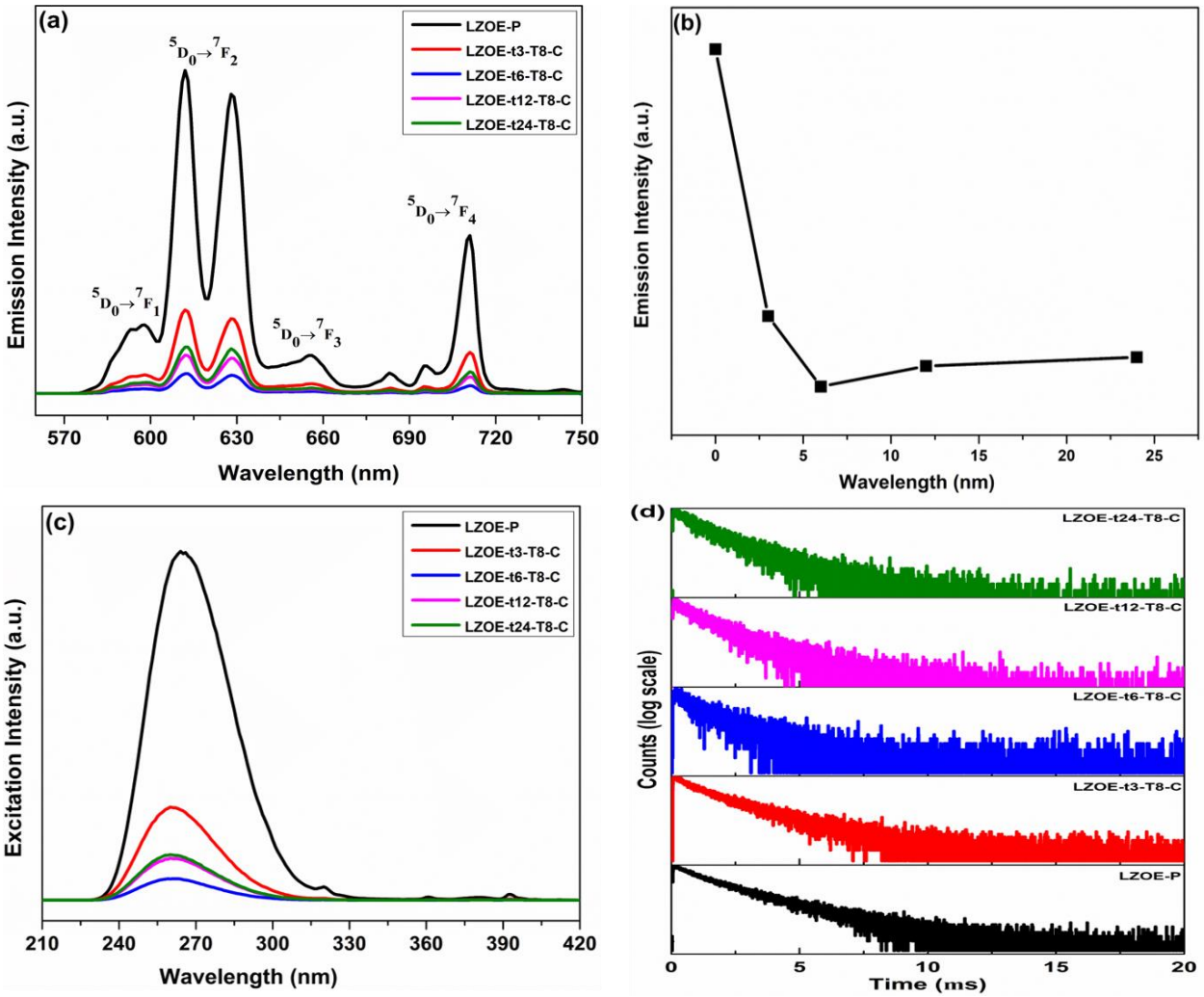

Figure 5. (a) Emission spectra (λ_{ex} = 260 nm), (b) variation of emission intensity as a function of processing time, (c) excitation spectra (λ_{em} = 612 nm), and (d) lifetime decay profiles of the preformed LZOE NPs with a control temperature processed at 800ºC in mixed sodium and potassium chloride medium with different molten-salt processing times.

To get an information about the ideal location of the dopant Eu^{3+} o in the LZO lattice sites, PL decay time (lifetime) studies were implemented. The decay curves (Figure 5d) corresponding to $^5D_0$ level of Eu^{3+} ions of the LZOE NPs depict monoexponentially outlines. This information tells us that Eu^{3+} ions were equally arranged in the LZOE NPs. As explained

before in emission data, Eu^{3+} ions are stabilized in the lattice which confirms the monoexponentially decay behavior. Additionally, there is not significant difference in the lifetime values for the preformed LZOE NPs and the molten-salt processed NPs for 3h (Table 1). The lifetime value originally got reduced from 3h to 6h and then increment further at 24h. The originally decrease in value at low durations was by agglomeration effects greater than surfaced defects whereas the opposite behavior prevails at increasing processing duration.

Molten-salt processing temperature

(Figure 6a) shows PL emission data where it was noted that a gradual decrease of emission intensity as molten-salt processing temperature increases. As discussed early, higher temperature creates particles to increase agglomeration which leads to scattering of light decreasing intensity. The second reason is thermal quenching that as temperature increases, thermal defects cause emission to decrease by creating nonradiative pathways. (Figure 6b) it is noted that the energy of charge transfer band increase by moving to shorter wavelength as processing temperature increases. This behavior is cause by increase of average distance between Eu^{3+} and surrounding anions making it difficult for electron transfer between oxygen and Eu due to extension of the crystal lattice. In both PL emission and excitation data proves the enhancement of the O→Eu charge transfer energy and thermal quenching of emission intensity as molten-salt processing temperature change. [68, 80]

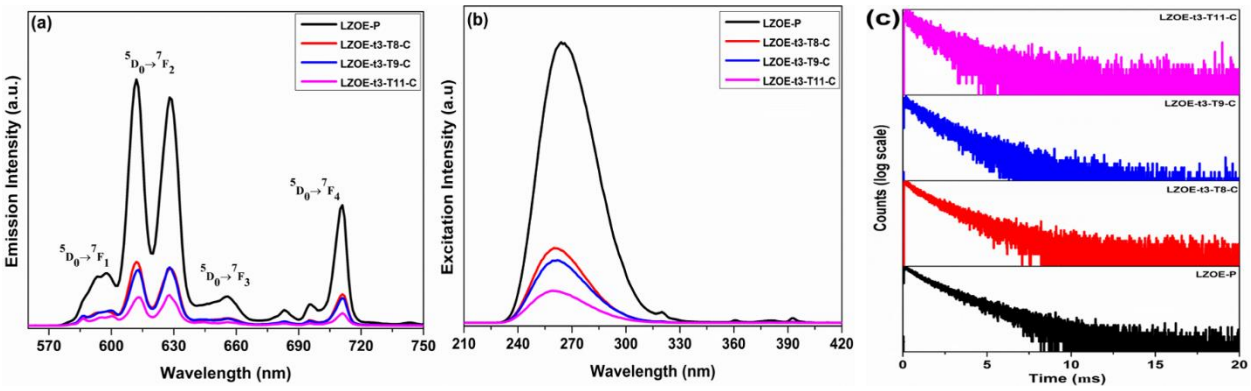

Figure 6. (a) Emission spectra (λ_{ex} = 260 nm), (b) excitation spectra (λ_{em} = 612 nm), and (c) lifetime decay profiles (λ_{ex} = 260 nm and (λ_{em} = 612 nm) of the preformed LZOE NPs with a control processed time at 3h in mixed sodium and potassium chloride medium with different molten-salt processing temperatures.

In (Figure 6c) molten-salt processing at different temperatures in lifetime decay show monoexponentially decay data which corresponds to $^5D_0$ level of Eu^{3+} ions. The lifetime value (Table 2) of LZOE NPs increases gradually with increase at 950ºC and then to some extent decreases at 1100ºC this behavior was attributed to surface area decrease at higher temperature and as particle size increases. As the surface area increase, increase of Eu^{3+} ions were rearranging close to the surface which leads to more defects that then quench fluorescence.

Molten-salt processing Medium

Molten-salt different mediums the emission (Figure 7a) and excitation spectra (Figure 7b) of the LZOE NPs show different intensities. In nitrate medium there is a higher emission and excitation in comparison with the chloride medium. Then when both mediums are compared with the preformed LZOE NPs the intensity in the preformed particles is higher. This behavior is attributed to the light scattering by agglomeration of nanoparticles since temperature is higher in chloride and a reprocess in nitrate medium which leads to agglomeration. (Table 3) lifetime

values obtained from the lifetime decay profiles (Figure 7c) show that the value for chloride medium is larger than in nitrate medium this is because the larger defect density for the latter in comparison with the former which show more dominant effect compared to agglomeration.

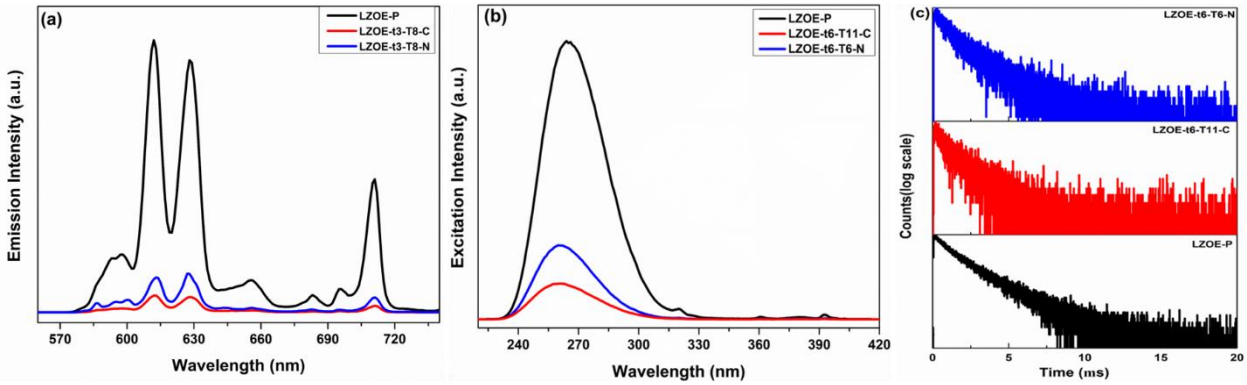

Figure 7. (a) Emission spectra (λ_{ex} = 260 nm), (b) excitation spectra (λ_{em} = 612 nm) (c) Lifetime decay profiles (λ_{ex} = 260 nm and λ_{em} = 612 nm) of preformed LZOE NPs after processed in the $NaNO_3$-KNO_3 and NaCl-KCl molten-salt media for 6h at 650^{o}C and 1100^{o}C.

Upconversion

For these phenomena, we describe two sequences of either doubly or triply doped $La_2Zr_2O_7$: NPs synthesized by a molten salt method. The first dopant sample is $La_2Zr_2O_7$:Yb,Er NPs, it is known that these dopants will displayed bright red and moderate green UC (VUC) and NIR-B DC (NDC) at around 1550 nm. For the second dopant sample, $La_2Zr_2O_7$:Gd,Yb,Tm NPs, displayed ultraviolet up-conversion (UVUC). In addition, we investigated the effects of sensitizer doping level on the morphology, crystal structure and UC and DC emission intensity of these NPs. [60]

4.1.5 X-Ray Diffraction Analysis

XRD data of $La_2Zr_2O_7$:Er,Yb NPs (Figure 8a) with different sensitizer concentrations and $La_2Zr_2O_7$: Yb, Tm, Gd NPs with control concentrations showed that no other extra peaks related to La_2O_3, Yb_2O_3, Er_2O_3, Tm_2O_3, Gd_2O_3 and ZrO_2 were noted meaning that the samples achieve high purity and no impurities were observed. XRD patterns matched pure $La_2Zr_2O_7$ phase with $Fm\bar{3}m$ space group and pyrochlore structure (JCPDS No. 78-1292). After calculating the crystallite size of all samples, it was noted in sample LZO:3%Er,x%Yb NPs (Table 4) that the size decrease as sensitizer concentration increase due to smaller ionic radius of 8-coordinated Yb^{3+} ion (98.6 pm) compared to 8-coordinated La^{3+} (116 pm).

Sample	Calculated Crystalline Size (nm)
LZO3Er0.25Yb	22.1 ± 0.9
LZO3Er0.50Yb	20.9 ± 0.9
LZO3Er0.75Yb	19.9 ± 0.9
LZO3Er1Yb	15.0 ± 1.1
LZO3Er2Yb	13.5 ± 1.1
LZO3Er5Yb	12.3 ± 1.2
LZO3Er7Yb	10.9 ± 1.3
LZO3Er10Yb	9.6 ± 1.4
LZO20Yb1Tm20Gd	20.5 ± 0.3

Table 4. Calculated crystallite size values of the LZO:3%Er, x%Yb NPs at various processing Yb^{3+} concentrations.

4.1.6 Raman Spectroscopy Analysis

Raman spectroscopy data shows both the doubly doped LZO:3%Er, x%Yb NPs and the triply doped LZO:20%Yb, 1.0%Tm, 20%Gd NPs adapting ideal pyrochlore phase showing the six peaks corresponding to the structure (Figure 8b). To study the extend of disordering from sample LZO:3%Er:x%Yb NPs and relationship with different concentrations of Yb^{3+} ions was done by variation of the full width half maxima (FWHM) of the most intense F_{2g} Raman peak located around 300 cm^{-1}. The gradual increase of the FWHM value (Figure 8b) shows the ordering extent of LZO:3%Er:x%Yb NPs with Yb^{3+} concentration increasing. This behavior is due to incorporation of Yb^{3+} ion from La^{3+} site to Zr^{4+} sites as Yb^{3+} concentration increase since the ionic

radius of 6-coordinated Zr^{4+} ion is 72 pm whereas that of Yb^{3+} ion is 98.6 pm causing a peak bordering with increase concentration. [81]

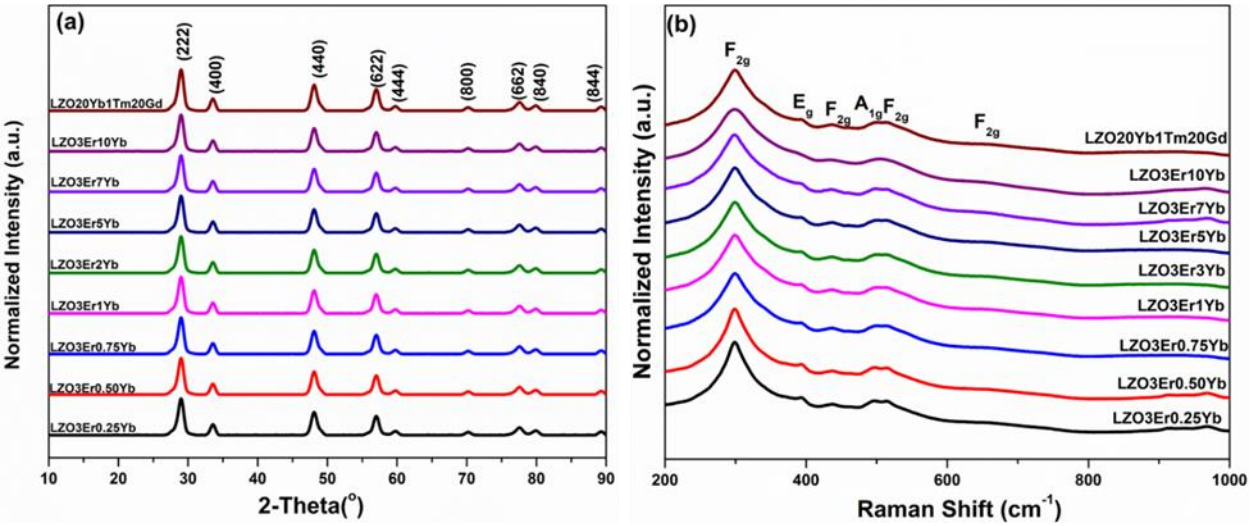

Figure 8. (a) XRD pattern (b) Raman spectra of LZO:3%Er, x%Yb NPs at various processing Yb^{3+} concentrations and LZO:20% Yb, 1.0% Tm, 20% Gd.

4.1.7 Scanning Electron Microscope

Scanning electron microscope (Figure 9a-g) shows the morphology and calculated particle size of the doubly doped LZO:3%Er:x%Yb NPs being with a spherical shape and equally dispersed with some agglomeration around particles. After calculations the size fall between a range of 10–35 nm, which decreases from 37 nm to 24 nm as processing concentrations of Yb^{3+} increases from 0.25% to 10%. The triply doped LZO:20%Yb,1.0%Tm,20%Gd NPs (Figure 9i) show sphere shape nanoparticles with an average particle size of ~43 nm. [76]

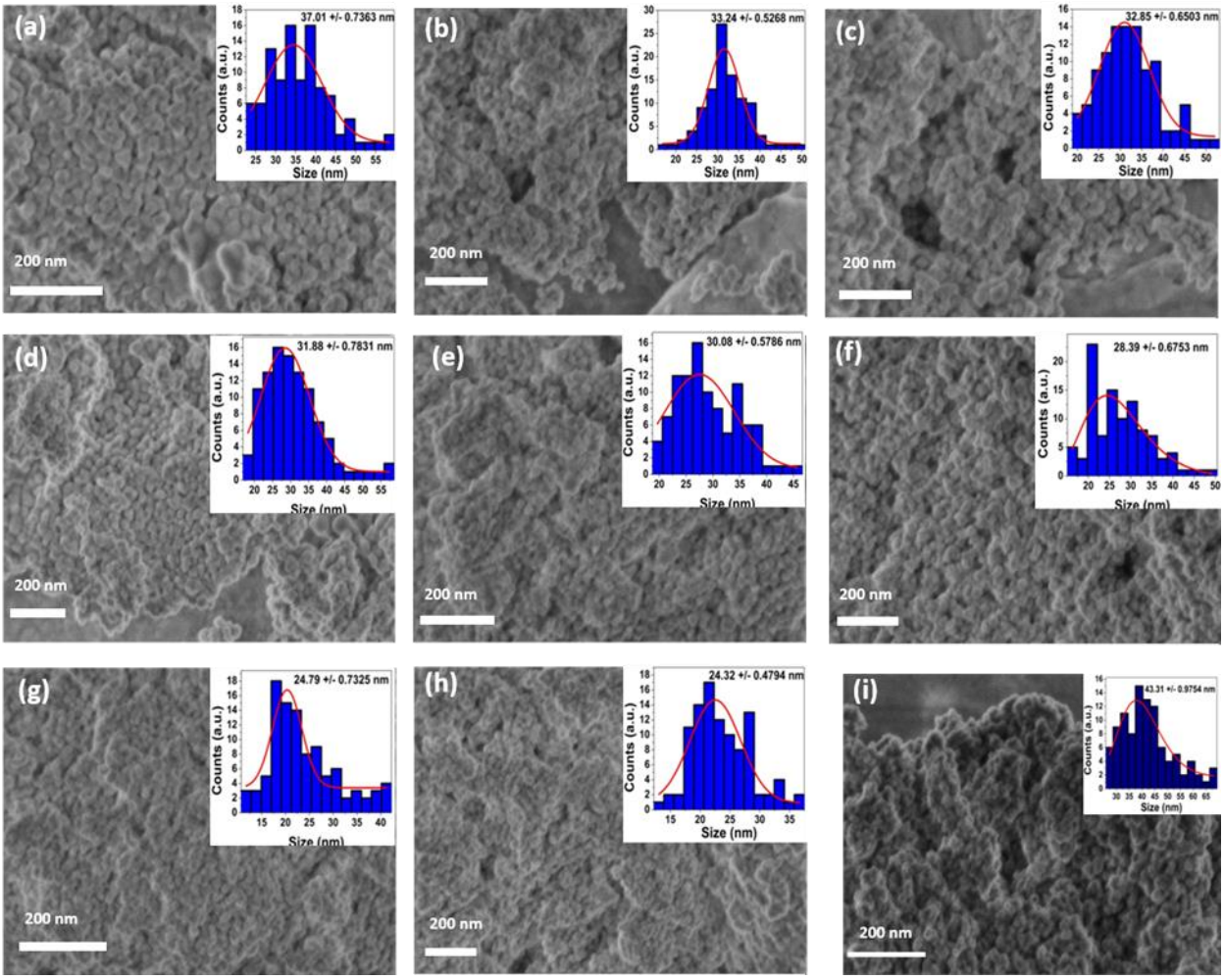

Figure 9. SEM images of LZO:3%Er,x%Yb NPs at various processing Yb^{3+} concentrations (a) 0.25%, (b) 0.50%, (c) 0.75%, (d) 1.0%, (e) 2.0%, (f) 5.0%, (g) 7.0%, (h) 10.0% and (i) LZO:20% Yb, 1.0% Tm, 20% Gd

4.1.8 Optical Analysis

NIR-Visible Up-conversion

The UC emission spectra (Figure 10a) of the LZO:Er,Yb NPs was analyze between 500-700 nm under 980 nm laser excitation. Three projecting peaks around 525, 550 and 660 nm are noted due to inter configurational f–f transitions of Er^{3+} ions. Moreover, double bands located at 525 and 550 nm in the green region are ascribed to $^{2}H_{11/2}$-$^{4}I_{15/2}$ and $^{4}S_{3/2}$-$^{4}I_{15/2}$ transitions of Er^{3+} ion. The higher intensity band in the red region around 660 nm is due to $^{4}F_{9/2}$-$^{4}I_{15/2}$ transition of Er^{3+} ion. The intensity ratio emission of the red and green emission bands increases up to 2.0% concentration and then decrease until 10.0% concentration (inset of Figure 10a). A relative UC emission spectrum for LZO:3%Er:x%Yb NPs with various processing concentrations of Er^{3+} ion was implemented (Figure 10b), the UC emission band intensity increase until 1.0% concentration and then decreasing encouraged by concentration quenching in the samples. [82, 83]

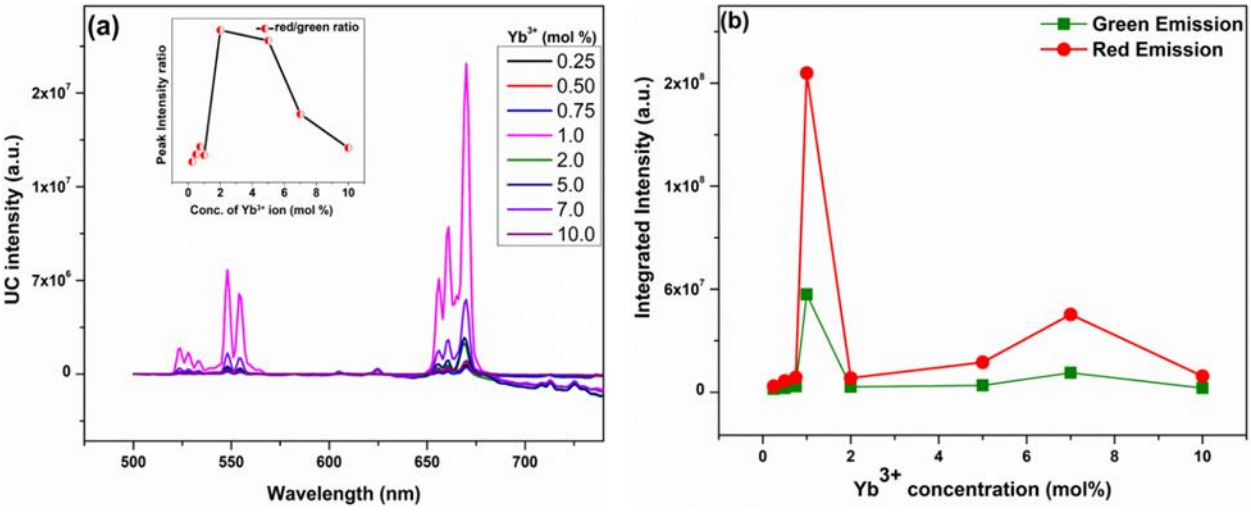

Figure 10. The LZO:Er,Yb NPs: (a) UC emission spectra and (b) variation of UC emission intensity at various processing Yb^{3+} concentration.

PL of the Triply Doped LZO:Yb,Tm,Gd NPs

In (Figure 11a); UVUC fluorescence data under 980 nm excitation LZO:20%Yb,1%Tm,20%Gd NPs displayed three emission peaks in a range of 260–284 nm are attributed to $^6I_J \rightarrow {}^8S_{7/2}$ transitions of Gd^{3+} ions. The emission peak position at 289 nm is assigned to $^3P_0/^1I_6 \rightarrow {}^3H_6$ transition of Tm^{3+} and emissions peaked at 296, 300, 306 nm are originated from $^6P_{5/2} \rightarrow {}^8S_{7/2}$, $^6P_{5/2} \rightarrow {}^8S_{7/2}$ and $^6P_{7/2} \rightarrow {}^8S_{7/2}$ transitions of Gd^{3+}ion, respectively. Energy levels diagram of Yb^{3+}, Gd^{3+}, and Tm^{3+} ions co-doped LZO NPs (Figure 11b) shows NIR photons are absorbed by the Yb^{3+} ions. Unlike Yb^{3+} ion, Gd^{3+} ions have a large energy gap between its ground state and excited state which cannot directly absorb 980 nm photons. Appropriately in a tridoped LZO NPs with Tm^{3+}, $Gd^{3+,}$ and Yb^{3+} ions, the energy transfer $^3P_{2,1} \rightarrow {}^3H_6(Tm^{3+}) : {}^8S_{7/2} \rightarrow {}^6I_j\,(Gd^{3+})$ populates the excited ^6I_j states of Gd^{3+}. Given that the probabiltiy of nonradiative transition from $^6I_{7/2}$ level to the $^6P_{5/2}$ level in Gd^{3+} is 5 times that of $^6I_{7/2} \rightarrow {}^8S_{7/2}$ radiative transition. We can conclude based on above discussion that the population of the $^3P_{1,2}$ levels is immensely important for strong UVUC from the LZO:20%Yb,1%Tm,20%Gd NPs.[84, 85]

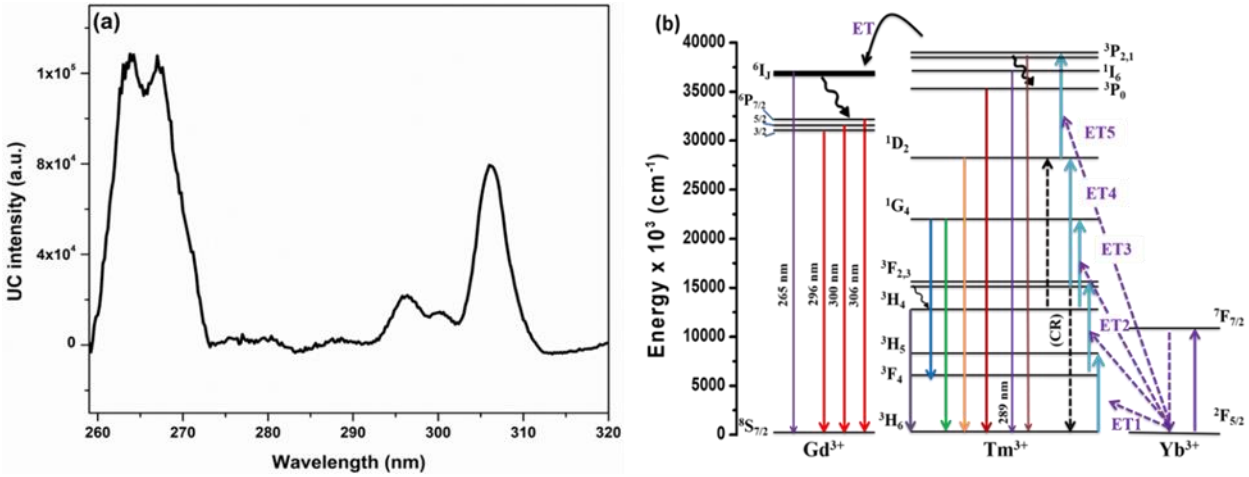

Figure 11. (a) UC emission spectra of LZO:20%Yb,1%Tm,20%Gd NPs and (b) Energy levels diagram of Yb^{3+}, Tm^{3+} and Gd^{3+} with likely mechanisms of the UC emissions.

CHAPTER V

CONCLUSION

5.1.1 Data conclusion

In this work, we highlighted the different downconversion and upconversion mechanisms through a simple controllable molten salt synthesis at different processing times, temperatures, salt mediums, or dopant concentrations. In this study LZO was ideal to investigate the pyrochlore phase under different parameters carried out by X-ray diffraction, Raman spectroscopy, scanning electron microscopy, and photoluminescence to investigate their size, shape, structure and optical property changes.

XRD show all samples to be pure since no other peaks were noted confirming purity. Crystallite size shows the size increases as time and temperature increases due to thermal quenching and more nucleation happening as these parameters increase. Raman spectroscopy concluded that all samples had a pyrochlore phase by portraying the six unique peaks (A_{1g} + E_g + $^4F_{2g}$) whereas temperature and time increases increase in crystal growth and higher lattice order. Morphology shows that increase in time and temperature leads to agglomeration and decrease lifetime value as the molten-salt processing time and temperature were raised due to decrease of defects under enhanced thermal condition. In Downconversion the best optimal time and temperature was 3 hours and 800 C due to least surface defects which causes the light to not scatter as much as at high temperatures or times which affects the luminescence intensity. For

different processes medium, Nitrate salts were better to obtain a well-define crystallize morphology and least surface defects on the samples. Chloride salts were best in increasing crystal growth.

In Upconversion, the effect of Yb^{3+} doping level was investigated on the UC intensity of the LZO:3%Er:x%Yb NPs. It was noted that as the Yb^{3+} concentration increase, the order degree of the pyrochlore phase and the particle size decreased. This was due to incorporation of Yb^{3+} into the lattice. The ionic radius of Yb^{3+} is smaller than La^{3+} causing a reduction on the particle size as the concentration increases. For the triple doped samples with Gd^{3+}, Tm^{3+}, and Yb^{3+} show that Tm^{3+} is efficiently populating on Gd^{3+} energy levels by making Gd^{3+} emitted luminescence at low wavelengths. In This work highlights the importance of post-synthesis thermal treatment conditions on tuning the size and structure of nanoparticles as well as LZO being an excellent pyrochlore material displaying visible UC which these behaviors are determined to help in science for bioimaging and water disinfection purposes.

REFERENCES

[1] M.J. Pitkethly, Nanomaterials–the driving force, Materials today 7(12) (2004) 20-29.

[2] G. Cao, Y. Wang, Nanostructures and nanomaterials: synthesis, Properties and Applications 2 (2004).

[3] A.S. Edelstein, R. Cammaratra, Nanomaterials: synthesis, properties and applications, CRC press1998.

[4] V. Pokropivny, R. Lohmus, I. Hussainova, A. Pokropivny, S. Vlassov, Introduction to nanomaterials and nanotechnology, Tartu University Press Tartu, Estonia2007.

[5] D.L. Fedlheim, C.A. Foss, Metal nanoparticles: synthesis, characterization, and applications, CRC press2001.

[6] S.K. Sahoo, R. Misra, S. Parveen, Nanoparticles: a boon to drug delivery, therapeutics, diagnostics and imaging, Nanomedicine in Cancer, Pan Stanford2017, pp. 73-124.

[7] C. Spinato, A.P.R. de Garibay, M. Kierkowicz, E. Pach, M. Martincic, R. Klippstein, M. Bourgognon, J.T.-W. Wang, C. Ménard-Moyon, K.T. Al-Jamal, Design of antibody-functionalized carbon nanotubes filled with radioactivable metals towards a targeted anticancer therapy, Nanoscale 8(25) (2016) 12626-12638.

[8] R. Paul, F. Du, L. Dai, Y. Ding, Z.L. Wang, F. Wei, A. Roy, 3D Heteroatom-Doped Carbon Nanomaterials as Multifunctional Metal-Free Catalysts for Integrated Energy Devices, Advanced Materials 31(13) (2019) 1805598.

[9] S. Govindaraju, M. Ramasamy, R. Baskaran, S.J. Ahn, K. Yun, Ultraviolet light and laser irradiation enhances the antibacterial activity of glucosamine-functionalized gold nanoparticles, International journal of nanomedicine 10(Spec Iss) (2015) 67.

[10] R. Gill, Superconductivity and ferromagnetism in nanomaterial NbSe2, AIP Conference Proceedings, AIP Publishing, 2017, p. 020041.

[11] X. Jiang, W. He, X. Zhang, Y. Wu, Q. Zhang, G. Cao, H. Zhang, J. Zheng, T.R. Croley, J.-J. Yin, Light-Induced Assembly of Metal Nanoparticles on ZnO Enhances the Generation of Charge Carriers, Reactive Oxygen Species, and Antibacterial Activity, The Journal of Physical Chemistry C 122(51) (2018) 29414-29425.

[12] S.K. Gupta, K. Sudarshan, P.S. Ghosh, K. Sanyal, A.P. Srivastava, A. Arya, P.K. Pujari, R.M. Kadam, Luminescence of undoped and Eu^{3+} doped nanocrystalline $SrWO_4$

scheelite: time resolved fluorescence complimented by DFT and positron annihilation spectroscopic studies, RSC Advances 6(5) (2016) 3792-3805.

[13] V.L. Colvin, The potential environmental impact of engineered nanomaterials, Nature biotechnology 21(10) (2003) 1166.

[14] N. Kamanina, NANOTECHNOLOGY IN OPTICS, CBU International Conference Proceedings, 2018, pp. 1114-1120.

[15] F. Zhong, J. Zhao, L. Shi, Y. Xiao, G. Cai, Y. Zheng, J. Long, Alkaline-Earth Metals-Doped Pyrochlore Gd 2 Zr 2 O 7 as Oxygen Conductors for Improved NO 2 Sensing Performance, Scientific reports 7(1) (2017) 4684.

[16] G. Ali, J.H. Lee, W. Chang, B.-W. Cho, H.-G. Jung, K.-W. Nam, K.Y. Chung, Lithium intercalation mechanism into FeF 3· 0.5 H 2 O as a highly stable composite cathode material, Scientific reports 7 (2017) 42237.

[17] C. Lu, Z. Lu, X. Wang, R. Xie, Z. Li, M. Higgins, C. Liu, F. Gao, L. Wang, Enhanced radiation-tolerant oxide dispersion strengthened steel and its microstructure evolution under helium-implantation and heavy-ion irradiation, Scientific reports 7 (2017) 40343.

[18] E. Omanović-Mikličanin, M. Maksimović, Nanosensors applications in agriculture and food industry, Bull Chem Technol Bosnia Herzegovina 47 (2016) 59-70.

[19] D. Oran, S.G. Rodriques, R. Gao, S. Asano, M.A. Skylar-Scott, F. Chen, P.W. Tillberg, A.H. Marblestone, E.S. Boyden, 3D nanofabrication by volumetric deposition and controlled shrinkage of patterned scaffolds, Science 362(6420) (2018) 1281-1285.

[20] N. Savage, M.S. Diallo, Nanomaterials and water purification: opportunities and challenges, Journal of Nanoparticle research 7(4-5) (2005) 331-342.

[21] E. Akdogan, R.E. Brennan, M. Allahverdi, A. Safari, Effects of molten salt synthesis (MSS) parameters on the morphology of Sr 3 Ti 2 O 7 and SrTiO 3 seed crystals, Journal of electroceramics 16(2) (2006) 159-165.

[22] Z. Li, X. Zhang, J. Hou, K. Zhou, Molten salt synthesis of anisometric $Sr_3Ti_2O_7$ particles, Journal of crystal growth 305(1) (2007) 265-270.

[23] K.H. Yoon, Y.S. Cho, D.H. Kang, Molten salt synthesis of lead-based relaxors, Journal of materials science 33(12) (1998) 2977-2984.

[24] J.P. Zuniga, S.K. Gupta, M. Abdou, Y. Mao, Effect of Molten Salt Synthesis Processing Duration on the Photo-and Radioluminescence of UV-, Visible-, and X-ray-Excitable $La_2Hf_2O_7$: Eu^{3+} Nanoparticles, ACS Omega 3(7) (2018) 7757-7770.

[25] J.P. Zuniga, M. Abdou, S.K. Gupta, Y. Mao, Molten-Salt Synthesis of Complex Metal Oxide Nanoparticles, JoVE (Journal of Visualized Experiments) (140) (2018) e58482.

[26] Z.F. Wang, M.J. Chen, Y. Ma, H. Liu, C.H. Han, X.T. Wang, Low-temperature molten salt synthesis of forsterite powders with controllable morphology, International Journal of Applied Ceramic Technology 14(1) (2017) 3-8.

[27] U. Manzoor, F.T. Zahra, S. Rafique, M.T. Moin, M. Mujahid, Effect of synthesis temperature, nucleation time, and postsynthesis heat treatment of ZnO nanoparticles and its sensing properties, Journal of Nanomaterials 16(1) (2015) 9.

[28] J.P. Zuniga, Molten-Salt Synthesized Pyrochlore Nanoparticles for Multifunctional Applications, The University of Texas Rio Grande Valley, 2019.

[29] X. Liu, N. Fechler, M. Antonietti, Salt melt synthesis of ceramics, semiconductors and carbon nanostructures, Chemical Society Reviews 42(21) (2013) 8237-8265.

[30] Y. Liu, L. Du, K. Gu, M. Zhang, Effect of Tm dopant on luminescence, photoelectric properties and electronic structure of In2S3 quantum dots, Journal of Luminescence 217 (2020) 116775.

[31] Y. Mao, X. Guo, J.Y. Huang, K.L. Wang, J.P. Chang, Luminescent nanocrystals with $A_2B_2O_7$ composition synthesized by a kinetically modified molten salt method, The Journal of Physical Chemistry C 113(4) (2009) 1204-1208.

[32] C. Rao, S. Vivekchand, K. Biswas, A. Govindaraj, Synthesis of inorganic nanomaterials, Dalton Transactions (34) (2007) 3728-3749.

[33] R. Srivastava, Synthesis and characterization techniques of nanomaterials, International Journal of Green Nanotechnology 4(1) (2012) 17-27.

[34] K.M. Turner, D.R. Rittman, R.A. Heymach, C.L. Tracy, M.L. Turner, A.F. Fuentes, W.L. Mao, R.C. Ewing, Pressure-induced structural modifications of rare-earth hafnate pyrochlore, Journal of Physics: Condensed Matter 29(25) (2017) 255401.

[35] S. Alizadeh, S. Hassanzadeh-Tabrizi, MoO3 fibers and belts: Molten salt synthesis, characterization and optical properties, Ceramics International 41(9) (2015) 10839-10843.

[36] H. Gao, K. Zhang, X. Teng, J. Li, Rolling Circle Amplification for Single Cell Analysis and in situ Sequencing, TrAC Trends in Analytical Chemistry (2019) 115700.

[37] D. Dorranian, A.F. Eskandari, Effect of Laser Fluence on the Characteristics of ZnO Nanoparticles Produced by Laser Ablation in Acetone, Molecular Crystals and Liquid Crystals 607(1) (2015) 1-12.

[38] M. Abdou, S.K. Gupta, J.P. Zuniga, Y. Mao, On structure and phase transformation of uranium doped $La_2Hf_2O_7$ nanoparticles as an efficient nuclear waste host, Materials Chemistry Frontiers 2(12) (2018) 2201-2211.

[39] S.B. Alaparthi, Y. Tian, Y. Mao, Synthesis and photoluminescence properties of $La_2Zr_2O_7$: Eu^{3+}@ YBO3 core@ shell nanoparticles, Nanotechnology 25(2) (2013) 025703.

[40] H. Xiang, Y. Chen, Energy-Converting Nanomedicine, Small 15(13) (2019) 1805339.

[41] N.M. Cepeda-Sánchez, J.A. Díaz-Guillén, M. Maczka, U. Amador, A.F. Fuentes, Cations size mismatch versus bonding characteristics: synthesis, structure and oxygen ion conducting properties of pyrochlore-type lanthanide hafnates, Journal of materials science 53(19) (2018) 13513-13529.

[42] T.Y. Fan, D.J. Ripin, R.L. Aggarwal, J.R. Ochoa, B. Chann, M. Tilleman, J. Spitzberg, Cryogenic Yb $^{3+} $-doped solid-state lasers, IEEE Journal of selected topics in Quantum Electronics 13(3) (2007) 448-459.

[43] S.K. Gupta, V. Grover, R. Shukla, K. Srinivasu, V. Natarajan, A. Tyagi, Exploring pure and RE co-doped (Eu3+, Tb3+ and Dy3+) gadolinium scandate: Luminescence behaviour and dynamics of energy transfer, Chemical Engineering Journal 283 (2016) 114-126.

[44] S. Gupta, J. Zuniga, P. Ghosh, M. Abdou, Y. Mao, Correlating Structure and Luminescence Properties of Undoped and $La_2Hf_2O_7$: Eu^{3+} NPs Prepared with Different Coprecipitating pH Values through experimental and theoretical studies, Inorg. Chem. 57 (2018) 11815-11830.

[45] S.K. Gupta, M. Abdou, P.S. Ghosh, J.P. Zuniga, Y. Mao, Thermally Induced Disorder–Order Phase Transition of $Gd_2Hf_2O_7$:Eu^{3+} Nanoparticles and Its Implication on Photo- and Radioluminescence, ACS Omega 4(2) (2019) 2779-2791.

[46] R.T. Wegh, H. Donker, K.D. Oskam, A. Meijerink, Visible quantum cutting in LiGdF4: Eu3+ through downconversion, Science 283(5402) (1999) 663-666.

[47] L. Wang, R.-J. Xie, T. Suehiro, T. Takeda, N. Hirosaki, Down-conversion nitride materials for solid state lighting: recent advances and perspectives, Chemical reviews 118(4) (2018) 1951-2009.

[48] Z. Wang, A. Meijerink, Dye-sensitized downconversion, The journal of physical chemistry letters 9(7) (2018) 1522-1526.

[49] R.D. Mehlenbacher, R. Kolbl, A. Lay, J.A. Dionne, Nanomaterials for in vivo imaging of mechanical forces and electrical fields, Nature Reviews Materials 3(2) (2018) 17080.

[50] Y.H. Kim, N.S. Viswanath, S. Unithrattil, H.J. Kim, W.B. Im, phosphor plates for high-power LED applications: challenges and opportunities toward perfect lighting, ECS Journal of solid state science and technology 7(1) (2018) R3134-R3147.

[51] C. Würth, S. Fischer, B. Grauel, A.P. Alivisatos, U. Resch-Genger, Quantum yields, surface quenching, and passivation efficiency for ultrasmall core/shell upconverting nanoparticles, Journal of the American Chemical Society 140(14) (2018) 4922-4928.

[52] P. Prabhakar Rao, K. Ajmal, K. Athira, T. Sreena, Influence of Morphology on Luminescence Properties of Xenotime-type Phosphors NaYP2O7: Eu3+ Synthesized via Solid State and Citrate-gel Routes, (2018).

[53] D.R. Cooper, J.A. Capobianco, J. Seuntjens, Radioluminescence studies of colloidal oleate-capped β-Na (Gd, Lu) F 4: Ln 3+ nanoparticles (Ln= Ce, Eu, Tb), Nanoscale 10(16) (2018) 7821-7832.

[54] S.K. Gupta, C. Reghukumar, R. Kadam, Eu^{3+} local site analysis and emission characteristics of novel $Nd_2Zr_2O_7$: Eu phosphor: insight into the effect of europium concentration on its photoluminescence properties, RSC Advances 6(59) (2016) 53614-53624.

[55] X. Min, Y. Sun, L. Kong, M. Guan, M. Fang, Y.g. Liu, X. Wu, Z. Huang, Novel pyrochlore-type $La_2Zr_2O_7$: Eu^{3+} red phosphors: Synthesis, structural, luminescence properties and theoretical calculation, Dyes and Pigments 157 (2018) 47-54.

[56] S.K. Gupta, C. Reghukumar, K. Sudarshan, P. Ghosh, N. Pathak, R. Kadam, Orange-red emitting $Gd_2Zr_2O_7$: Sm^{3+}: Structure-property correlation, optical properties and defect spectroscopy, Journal of Physics and Chemistry of Solids 116 (2018) 360-366.

[57] S.K. Gupta, J.P. Zuniga, M. Abdou, Y. Mao, Thermal annealing effects on $La_2Hf_2O_7$: Eu^{3+} nanoparticles: a curious case study of structural evolution and site-specific photo-and radio-luminescence, Inorganic Chemistry Frontiers 5(10) (2018) 2508-2521.

[58] J. Honig, J. Spałek, Electronic Properties of NiS_2-x Se x Single Crystals: From Magnetic Mott− Hubbard Insulators to Normal Metals, Chemistry of materials 10(10) (1998) 2910-2929.

[59] M.A.P. Garcia, S.K. Gupta, Y. Mao, Effects of molten-salt processing parameters on the structural and optical properties of preformed La2Zr2O7: Eu3+ nanoparticles, Ceramics International (2019).

[60] S.K. Gupta, M.A.P. Garcia, J.P. Zuniga, M. Abdou, Y. Mao, Visible and ultraviolet upconversion and near infrared downconversion luminescence from lanthanide doped La2Zr2O7 nanoparticles, Journal of Luminescence 214 (2019) 116591.

[61] A.V. Rane, K. Kanny, V. Abitha, S. Thomas, Methods for Synthesis of Nanoparticles and Fabrication of Nanocomposites, Synthesis of Inorganic Nanomaterials, Elsevier2018, pp. 121-139.

[62] R. Piticescu, C. Monty, D. Taloi, A. Motoc, S. Axinte, Hydrothermal synthesis of zirconia nanomaterials, Journal of the European Ceramic Society 21(10-11) (2001) 2057-2060.

[63] M.K. Devaraju, I. Honma, Hydrothermal and solvothermal process towards development of LiMPO4 (M= Fe, Mn) nanomaterials for lithium-ion batteries, Advanced Energy Materials 2(3) (2012) 284-297.

[64] I. Pidchenko, K.O. Kvashnina, T. Yokosawa, N. Finck, S. Bahl, D. Schild, R. Polly, E. Bohnert, A. Rossberg, J.r. Göttlicher, Uranium redox transformations after U (VI) coprecipitation with magnetite nanoparticles, Environmental science & technology 51(4) (2017) 2217-2225.

[65] P.A. Vinosha, L.A. Mely, J.E. Jeronsia, S. Krishnan, S.J. Das, Synthesis and properties of spinel ZnFe2O4 nanoparticles by facile co-precipitation route, Optik 134 (2017) 99-108.

[66] K.K. Rao, T. Banu, M. Vithal, G. Swamy, K.R. Kumar, Preparation and characterization of bulk and nano particles of $La_2Zr_2O_7$ and $Nd_2Zr_2O_7$ by sol–gel method, Materials Letters 54(2-3) (2002) 205-210.

[67] J.P. Zuniga, S.K. Gupta, M. Pokhrel, Y. Mao, Exploring the optical properties of $La_2Hf_2O_7$: Pr^{3+} nanoparticles under UV and X-ray excitation for potential lighting and scintillating applications, New Journal of Chemistry 42(12) (2018) 9381-9392.

[68] W. Xiaoyong, Y. Liang, L. Mingyu, C. Rui, L. Yongzhou, Synthesis and fluorescence properties of Y_2O_3: Eu by molten salt synthesis method, Journal of Rare Earths 28(5) (2010) 688-692.

[69] J. Wang, Y. Song, Microfluidic synthesis of nanohybrids, Small 13(18) (2017) 1604084.

[70] B. Zhou, B. Shi, D. Jin, X. Liu, Controlling upconversion nanocrystals for emerging applications, Nature nanotechnology 10(11) (2015) 924.

[71] E. Leroy, H. Lami, G. Laustriat, FLUORESCENCE LIFETIME AND QUANTUM YIELD OF PHENYLALANINE AQUEOUS SOLUTIONS. TEMPERATURE AND CONCENTRATION EFFECTS, Photochemistry and Photobiology 13(5) (1971) 411-421.

[72] Y.-Y. Zhang, Y.-F. Hua, Z.-Y. Deng, Driven self-assembly of hard nanoplates on soft elastic shells, Chinese Physics B 24(11) (2015) 118202.

[73] N.A.A. Mohd Arif, C.C. Jiun, S. Shaari, Effect of Annealing Temperature and Spin Coating Speed on Mn-Doped ZnS Nanocrystals Thin Film by Spin Coating, Journal of Nanomaterials 2017 (2017) 6.

[74] A. Muradova, M. Zaytseva, A. Sharapaev, E. Yurtov, Influence of temperature and synthesis time on shape and size distribution of Fe3O4 nanoparticles obtained by ageing method, Colloids and Surfaces A: Physicochemical and Engineering Aspects 509 (2016) 229-234.

[75] J.I. Goldstein, D.E. Newbury, J.R. Michael, N.W. Ritchie, J.H.J. Scott, D.C. Joy, Scanning electron microscopy and X-ray microanalysis, Springer2017.

[76] E. Smith, G. Dent, Modern Raman spectroscopy: a practical approach, Wiley2019.

[77] S. Nandi, Y. Jana, S. Sarkar, R. Jana, G. Mukherjee, H. Gupta, Synthesis, structure, UV–Vis–NIR, infrared and Raman spectroscopy, and force-field investigation for A2GaSbO7 (A3+= Y, Dy, Gd) pyrochlores, Journal of Alloys and Compounds 771 (2019) 89-99.

[78] X. Qin, X. Liu, W. Huang, M. Bettinelli, X. Liu, Lanthanide-activated phosphors based on 4f-5d optical transitions: theoretical and experimental aspects, Chemical reviews 117(5) (2017) 4488-4527.

[79] N.S. Singh, R. Ningthoujam, M.N. Luwang, S.D. Singh, R. Vatsa, Luminescence, lifetime and quantum yield studies of YVO4: Ln3+ (Ln3+= Dy3+, Eu3+) nanoparticles: Concentration and annealing effects, Chemical Physics Letters 480(4-6) (2009) 237-242.

[80] L. Vradman, J. Zana, A. Kirschner, M. Herskowitz, Synthesis of LaMnO 3 in molten chlorides: effect of preparation conditions, Physical Chemistry Chemical Physics 15(26) (2013) 10914-10920.

[81] S.K. Gupta, J.P. Zuniga, M. Abdou, Y. Mao, Thermal annealing effects on La 2 Hf 2 O 7: Eu 3+ nanoparticles: a curious case study of structural evolution and site-specific photo- and radio-luminescence, Inorganic Chemistry Frontiers 5(10) (2018) 2508-2521.

[82] R. Perrella, I. Ribeiro, P. Campos-Junior, M. Schiavon, E. Pecoraro, S. Ribeiro, J. Ferrari, CaTiO3: Er3+: Yb3+ upconversion from 980 nm to 1550 nm excitation and its potential as cells luminescent probes, Materials Chemistry and Physics 223 (2019) 391-397.

[83] K. Welsher, Z. Liu, S.P. Sherlock, J.T. Robinson, Z. Chen, D. Daranciang, H. Dai, A route to brightly fluorescent carbon nanotubes for near-infrared imaging in mice, Nature nanotechnology 4(11) (2009) 773.

[84] X. Chen, Z. Song, Study on six-photon and five-photon ultraviolet upconversion luminescence, JOSA B 24(4) (2007) 965-971.

[85] J. Sytsma, G. Imbusch, G. Blasse, The decay of the 6I7/2 term level of Gd3+ in YOCl and LiYF4, Journal of Physics: Condensed Matter 2(23) (1990) 5171.

BIOGRAPHICAL SKETCH

Ms. Mitzy A. Penilla Garcia was born in 1991 in Guadalajara, Mexico. She received her Bachelor's in Science with the Biology program (2016) at the University of Texas Rio Grande Valley. She joined the Multifunctional Applications of Oxides (MAO) Nano Laboratory were she begin her research career as a scientist. Her work focusing on Inorganic chemistry lead her to publish several journal articles. She received awards such as J. Lell Elliot, Welch's Foundation, USDA, and HSF for her work in research. She also received first place on Partnership for Research and Education in Material Science (PREM) Conference for her work "Effects of Molten-Salt processing on structural and optical properties of preformed $La_2Zr_2O_7:Eu^{3+}$ nanoparticles." She received her Master of Science in Chemistry diploma from the University of Texas Rio Grande Valley in May 2020. She is looking for a prosperous and bright future in the coming years as her role as a scientist. For more information; please contact her at email:mitzygarcia@live.com